Measuring and modeling investigation of the Net Photochemical Ozone Production Rate via an improved dual-channel reaction chamber technique

Yixin Hao[1,2#], Jun Zhou[1,2#*], Jie-Ping Zhou[1,2], Yan Wang[1,2], Suxia Yang[1,2], Yibo Huangfu[1,2], Xiao-Bing Li[1,2], Chunsheng Zhang[3], Aiming Liu[3], Yanfeng Wu[1,2], Yaqing Zhou, Shuchun Yang[1,2], Yuwen Peng[1,2], Jipeng Qi[1,2], Xianjun He[1,2], Xin Song[1,2], Yubin Chen[1,2], Bin Yuan[1,2*], Min Shao[1,2]

[1]Institute for Environmental and Climate Research, Jinan University, Guangzhou 511443, China

[2]Guangdong-Hongkong-Macau Joint Laboratory of Collaborative Innovation for Environmental Quality, Guangzhou 511443, China

[3]Shenzhen National Climate Observatory, Shenzhen 518040, China

[#]Yixin Hao and Jun Zhou contribute equally to this work.

Correspondence to: Jun Zhou (Junzhou@jnu.edu.cn) and Bin Yuan (byuan@jnu.edu.cn)

Abstract. Current process-based research mainly uses box models to evaluate the photochemical ozone production and destruction rates, and it is not clear to what extent the photochemical reaction mechanisms are understood. Here, we modified and improved a net photochemical ozone production rate (NPOPR, $P(O_3)_{net}$) detection system based on the current dual-channel reaction chamber technique, which makes the instrument applicable to different ambient environments, and its various operating indicators were characterized, i.e., airtightness, light transmittance, wall losses of the reaction and reference chambers, conversion rate of O_3 to NO_2, air residence time, and performance of the reaction and reference chambers. The limits of detection of the NPOPR detection system were determined to be 0.07, 1.4, and 2.3 ppbv h^{-1} at sampling flow rates of 1.3, 3, and 5 L min^{-1}, respectively. We further applied the NPOPR detection system to field observations at an urban site in the Pearl River Delta (China). During the observation period, the maximum value of $P(O_3)_{net}$ was 34.1 ppbv h^{-1}, which was $\sim$ 0 ppbv h^{-1} at night within the system detection error and peaked at approximately noon local time. The daytime (from 6:00–18:00) average value of $P(O_3)_{net}$ was 12.8 ($\pm$5.5) ppbv h^{-1}. We investigated the detailed photochemical O_3 formation mechanism in the reaction and reference chambers of the NPOPR detection system using a zero-dimensional box model. We found that the photochemical reactions in the reaction chamber were very close to those in ambient air, but it was not zero chemistry in the reference chamber, the reaction related to the production and destruction of RO_2 (=HO_2+RO_2) continued in the reference chamber, which

33   led to a small amount of $P(O_3)_{net}$. Therefore, the $P(O_3)_{net}$ measured here can be regarded as the lower

34   limit of the real $P(O_3)_{net}$ in the atmosphere; however, the measured $P(O_3)_{net}$ was still ~ 7.5 to 9.3 ppbv h^{-}

35   ^{1} higher than the modeled $P(O_3)_{net}$ value depending on different modeling methods, which may be due to

36   the inaccurate estimation of HO_2/RO_2 radicals in the modeling study. Short-lived intermediate

37   measurements coupled with direct $P(O_3)_{net}$ measurements are needed in the future to better understand

38   O_3 photochemistry. Our results show that the NPOPR detection system can achieve high temporal

39   resolution and continuous field observations, which helps us to better understand photochemical O_3

40   formation and provides a key scientific basis for continuous improvement of air quality in China.

41

42

1 Introduction

Surface O_3 pollution has become a major challenge in air quality management in China (Shen et al., 2021). Elevated surface O_3 mixing ratios exert severe adverse effects on public health, such as respiratory diseases, and the estimated annual mortality attributable to surface O_3 exposure exceeds 150,000 deaths in China (Malley et al., 2017). O_3 pollution is also detrimental to key staple crop yields, reducing the yields of wheat, soybean, and maize by up to 15 %, and is threatening global food security (Avnery et al., 2011; Mills et al., 2018; Karakatsani et al., 2010; Berman et al., 2012; O'Neill et al., 2003). As a greenhouse gas, O_3 also contributes significantly to climate change (Bell et al., 2004). With the rapid economic development and urbanization in the Pearl River Delta (PRD) region in China, O_3 pollution is pretty severe, especially in summer and autumn (Zou et al., 2015; Zhang et al., 2021).

The variation in O_3 in the planetary boundary layer is predominantly influenced by deposition, advection transport, vertical mixing (i.e., entrainment from the stratosphere), meteorological factors, and chemical reactions. Therefore, the O_3 budget in the boundary layer can be expressed as Eq. (1):

$$\frac{\partial [O_3]}{\partial t} = \underbrace{P(O_3) - D(O_3)}_{P(O_3)_{net}} \underbrace{- \frac{v}{H}[O_3]}_{SD} + \underbrace{u_i \frac{\partial [O_3]}{\partial x_i}}_{A} + STE \tag{1}$$

where SD, A, and STE represent the surface deposition, advection, and stratosphere-troposphere exchange (STE), respectively; $[O_3]$, $P(O_3)$ and $D(O_3)$ are the ambient O_3 mixing ratios, photochemical O_3 production and its loss rate, respectively; v, H, and u_i represent the O_3 deposition velocity, mixing layer height, and velocity in three directions, respectively; and A consists of u_i times the O_3 gradient in those three directions.

Tropospheric O_3 is a key component of photochemical smog, mainly formed by photochemical reactions of nitrogen oxides ($NO_x=NO+NO_2$) and volatile organic compounds (VOCs) (Lee et al., 2010). The specific process of the photochemical reaction is the photolysis of NO_2 at < 420 nm to generate $O(^3P)$ atoms, thereby promoting the formation of O_3 (Sadanaga et al., 2017). Simultaneously, there is a RO_X ($RO_X = OH + HO_2 + RO_2$) radical cycle in the troposphere, which continuously provides HO_2 and RO_2 to oxidize NO to NO_2 resulting in the accumulation of O_3 (Shen et al., 2021; Sadanaga et al., 2017; Cazorla et al., 2010).

Typical meteorological scenarios for the occurrence of O_3 pollution episodes in polluted urban

71 centers are usually characterized by weak winds, strong solar radiation, and high temperature (T). Under

72 such conditions, local formation of O_3 plays a crucial role in the rapid increase of surface O_3 in daytime.

73 In addition, in Eq. (1), the surface deposition and advection of O_3 are proportional to ambient O_3 mixing

74 ratios, [O_3], which is mainly generated by local photochemistry (Carzorla et al., 2010). If $P(O_3)_{net}$ can be

75 reduced by regulatory measures, overall O_3 levels will decline proportionately over time (Cazorla et al.,

76 2010), thus, the investigation of $P(O_3)_{net}$ formation mechanism is urgently needed.

77   Current studies on $P(O_3)_{net}$ estimation mainly rely on modeling methods, the gas-phase chemical

78 mechanisms were frequently used to identify key drivers of O_3 pollution events and provide guidance for

79 making effective O_3 reduction strategies, such as the Master Chemical Mechanism (MCM), the regional

80 atmospheric chemistry mechanism (RACM), the Carbon Bond mechanisms (CBM) and the Mainz

81 Organic Mechanism (MOM) (Shen et al., 2021; Kanaya et al., 2016; Wang et al., 2014; Tadic et al.,

82 2020; Ren et al., 2013; Lu et al., 2010; Zhou et al., 2014; Mazzuca et al., 2016). However, uncertainties

83 in emission inventories, chemical mechanisms, and meteorology make it difficult to perfectly reproduce

84 real atmospheric processes, which can lead some bias in modeling the $P(O_3)_{net}$. According to the existing

85 field observations, researchers found that the mixing ratios of HO_2 or RO_2 obtained from the model

86 simulation was inconsistent with that obtained from the direct measurement, leading to the deviation of

87 $P(O_3)_{net}$ between observation and model simulation results (Wang et al., 2014; Tadic et al., 2020; Ren et

88 al., 2013; Martinez et al., 2003). Therefore, we urgently need a method that can directly measure the

89 $P(O_3)_{net}$.

90   Recently, researchers have developed sensors that can directly measure $P(O_3)_{net}$ in the atmosphere

91 using the dual-channel chamber technique (Sadanaga et al., 2017; Cazorla et al., 2010; Baier et al., 2015

92 and 2017; Sklaveniti et al., 2018), where ambient air is introduced into two chambers of identical size,

93 one UV transparent chamber (reaction chamber) and one UV protection chamber (reference chamber).

94 In the presence of solar UV light, O_3 is produced by photochemical reactions in the reaction chamber,

95 but not in the reference chamber. The system does not directly measure O_3 mixing ratios, it measures the

96 combined mixing ratios of O_3 and nitrogen dioxide (NO_2). $P(O_3)_{net}$ is determined by the difference of

97 $O_X(O_X=O_3+NO_2)$ mixing ratios between the reaction and reference chambers. These studies have greatly

98 helped us to understand the O_3 photochemical formation mechanism, but defects still exists in current

99 studies, for example, the sensors developed by Cazorla et al. (2010) and Baier et al. (2015) both have an

NO$_2$-to-O$_3$ converter unit, and uses a modified O$_3$ monitor (Thermo Scientific, Model 49i, USA) to measure Ox, but the zero point of the O$_3$ monitor is easy to drift, together with the limitation of the conversion efficiency of NO$_2$ to O$_3$ (~ 99.9 %) and the effects of the T and relative humidity (RH) to O$_3$ monitor, this method can introduce large measurement uncertainties. Sklaveniti et al. (2018) have shorten the average residence time in the chambers to 4.5 min, which reduced the scattering and increased the time resolution of ΔOx measurement, but large wall loss still exists in their system, which are 5 % and 3 % for O$_3$ and NO$_2$, respectively. Sadanaga et al. (2017) passed the NO standard gas into the PFA tube to convert O$_3$ into NO$_2$ to detect Ox, which is easy to operate, but the LIF-NO$_2$ detector is less portable and maintainable. Furthermore, all the current sensors have different degrees of wall loss of NO$_2$ and O$_3$ that can even reach 15 %, which largely affect the accuracy of the evaluation of $P(O_3)_{net}$.

In this study, we modified and improved a $P(O_3)_{net}$ sensor based on the dual-channel technique as described above and named it the net photochemical ozone production rate (NPOPR) detection system. Section 2 provides the improvement and characterization of the NPOPR detection system. Furthermore, we applied the NPOPR detection system to an observation campaign conducted at Shenzhen Meteorological Gradient Tower (SZMGT) in the Pearl River Delta (PRD) region in China. A zero-dimensional box model based on the Framework for 0-D Atmospheric Modeling (F0AM) v3.2 coupled with MCM v3.3.1 was used to simulate the photochemical reactions inside both the reaction and reference chambers in the NPOPR system, which allowed us to assess the ability of the current modeling method to model $P(O_3)_{net}$, as described in Sect. 3. The current research could help us study the source and formation mechanism of O$_3$ and provide effective theoretical support for the prevention and control of O$_3$ pollution. Because the system can directly obtain real-time $P(O_3)_{net}$ under different environmental conditions, it can meet richer and more specific research needs.

2 Method and materials

2.1 Development of the NPOPR detection system

A schematic and actual diagram of the NPOPR detection system are shown in Fig. 1. The integral construction is similar to the P-L(Ox) measurement system built by Sadanaga et al. (2017) and Sklaveniti et al. (2018), which mainly consists of reaction and reference chambers with the same geometry and made of quartz (190.5 mm inner diameter and 700 mm length; more details can be found in Fig. S1). To

128 prevent photochemical reactions inside the reference chamber, an ultraviolet (UV) protection Ultem film

129 (SH2CLAR, 3 M, Japan) was used to cover the outer surface to block sunlight with wavelengths < 390

130 nm. During the experiment, both the reaction and reference chambers were located outdoors and exposed

131 to sunlight directly to simulate genuine ambient photochemistry reactions. Ambient air was introduced

132 into the reaction and reference chambers at the same flow rate, and a Teflon filter was mounted before

133 the chamber inlet to remove fine particles. A stream of air from the two chambers was alternately

134 introduced into an NO-reaction chamber every 2 min to convert O_3 in the air to NO_2 in the presence of

135 high mixing ratios of NO ($O_3+NO=NO_2$), and the Ox mixing ratios from the outlet NO-reaction chamber,

136 i.e., the total NO_2 mixing ratios including the inherent NO_2 in the ambient and that converted from O_3,

137 were measured by a Cavity Attenuated Phase Shift (CAPS) NO_2 Monitor (Aerodyne research, Inc.,

138 Billerica MA, USA) to avoid other nitrogen oxide interferences to the NO_2 measurement (such as alkyl

139 nitrates, peroxyacyl nitrates, peroxynitric acid, nitrogen pentoxide, etc.). Compared to previous studies

140 that used a dual-channel UV-absorption O_3 monitor (Cazorla et al., 2010) or a laser-induced fluorescence

141 (LIF) LIF-NO_2 monitor (Sadanaga et al., 2017) for Ox measurements, our choice could make the NPOPR

142 detection system have a more stable zero-baseline and be more portable by assembling each part together,

143 i.e., put the CAPS NO_2 monitor, the automatic sampling system, and the automatic data sampling system

144 onto the indoor cabinets with the push-pull base, and put the dual chambers onto the outdoor shelf with

145 the push-pull base. Additionally, we modified the air sampling system to adjust the total air flow rates

146 freely from 1.3 to 5 L min^{-1} in the reaction and reference chambers, which enabled us to achieve different

147 air residence times from 3.8 to 21 min. This time range covered all the residence times from previous

148 studies using different Ox measurement techniques, which ranged from 4.5 to 20.5 min (Cazorla et al.,

149 2010; Baier et al., 2015; Sadanaga et al., 2017; Sklaveniti et al., 2018). According to the simulation

150 results described in Sect. 3, the reaction rates of O_3 formation and destruction pathways and the radicals

151 that play critical roles in photochemical O_3 formation, such as HO_2, RO_2 and OH, reached quasi-steady

152 states in approximately 3 min, so it was reasonable for us to set the air flow rate highest at 5 L min^{-1},

153 where the sampled air has already reacted for 3.8 min in the reaction and reference chambers. On the

154 other hand, this also demonstrated that it was reasonable to set the alternate sampling time for the reaction

155 and reference chambers at 2 min, where the sampled air actually has already reacted for at least 3.8 min

156 in the reaction and reference chambers. The switch system was controlled by two Teflon three-way

157 solenoid valves (001-0028-900, Parker, GER) located before the NO-reaction chamber (see Fig. 1). We

158 used homemade circuit control software (Four-Channel-Valves boxed) and a solenoid valve (001-0028-

159 900, Parker, GER) to automatically switch the sampling lines every 2 min. To keep the flow rates in the

160 reaction and reference chambers the same and avoid gas flow accumulation in the chamber, a pump

161 (pump 3) was connected to the Teflon three-way solenoid valves in parallel to the NO-reaction chamber

162 to evacuate the air that was not introduced into the NO-reaction chamber. To reduce NO interference, the

163 system used O_X to infer the amount of O_3 generated by photochemical reactions (Liu et al., 1977; Pan et

164 al., 2015; Lu et al., 2010). The difference between the Ox mixing ratios in the reaction and reference

165 chambers, denoted by ΔOx, represents the amount of O_3 generated by the photochemical reaction.

166 $P(O_3)_{net}$ was obtained by dividing ΔOx by the average residence time of air in the reaction chamber $\langle \tau \rangle$:

167 $$P(O_3)_{net} = P(O_X) = \frac{\Delta O_X}{\tau} = \frac{[O_X]_{reaction} - [O_X]_{reference}}{\tau}$$ (2)

168   Igor Pro version 6 was used to calculate $P(O_3)_{net}$ as follows: ① separate the data of the reaction

169 and the reference chambers into two sets using the recorded valve number of 1 (reaction chamber) and 0

170 (reference chamber) during the sampling time; ② for each 2 min period of data, delete the first 20 s and

171 the last 20 s when the signal was not stable, then average the rest data, and do the interpolate calculation

172 of the reference chamber dataset; ③ calculate the difference between the Ox mixing ratios in the reaction

173 and reference chambers (i.e., ΔO_X) at the time when the reaction chamber measured Ox; ④ divide ΔO_X

174 by the average residence time of air in the reaction chamber $\langle \tau \rangle$ and obtain $P(O_3)_{net}$ at a time resolution

175 of 4 min.

(a)

(b)
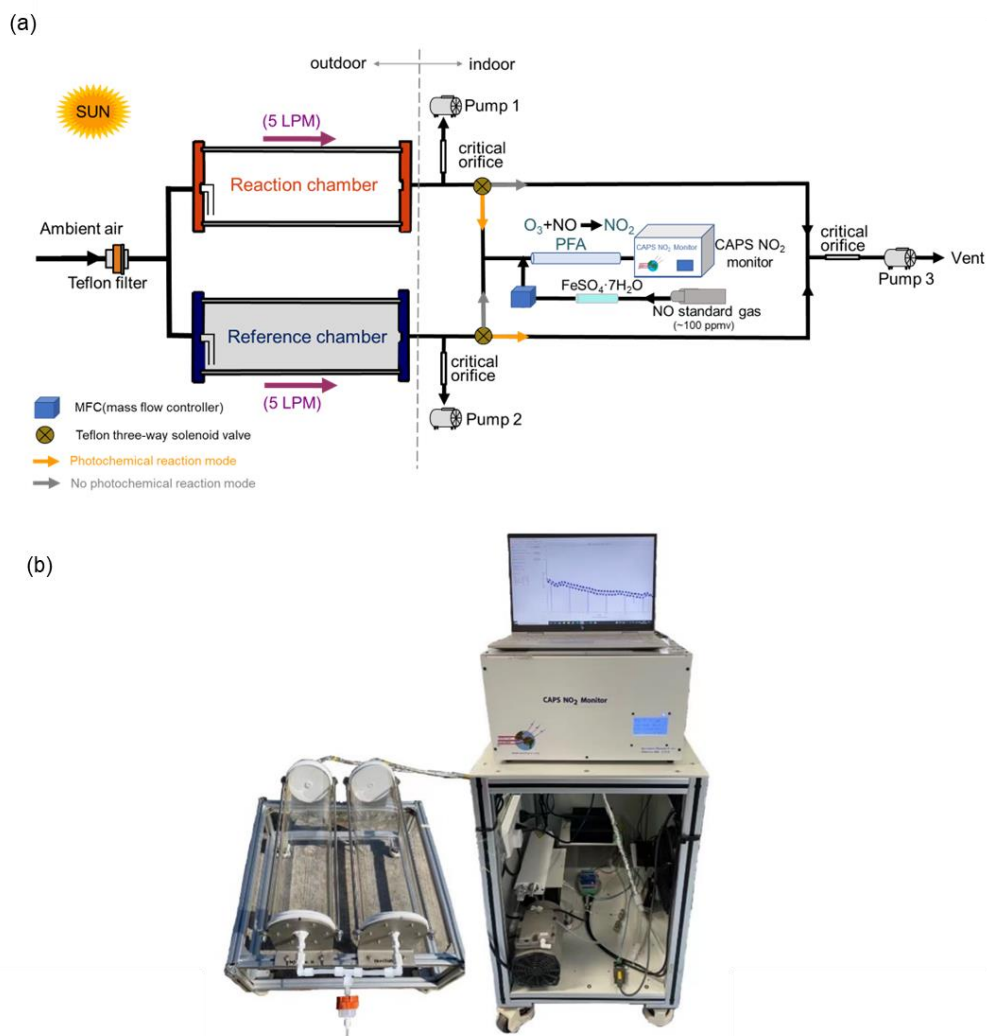
177 **Figure 1: (a) Schematic and (b) actual diagram of the NPOPR detection system.**

178   The major improvements of the NPOPR detection system described here compared to previous

179 studies to optimize $P(O_3)_{net}$ measurements are as follows: (1) we improved the design of the reaction and

180 reference chambers to ensure that they have good airtightness, which will increase the measurement

181 accuracy of different species inside the chambers. More details can be found in Sect. 2.2 and Appendix

182 I; (2) two pumps (labeled pump 1 and pump 2 in Fig. 1) were added directly after the reaction and

183 reference chambers to continuously draw ambient air through the two chambers (as the makeup flow) to

184 adjust the total air flow rates freely from 1.3 to 5 L min^{-1} in the chambers. By doing this, we were able

185 to achieve different limits of detection (LODs) of the NPOPR system (see Sect. 2.4), making the

186 instrument applicable to different ambient environments, i.e., in highly polluted areas, we could use

187 higher air flow rates to reduce the wall loss effects of the chambers, and in less polluted areas, we could

188 use lower flow rates to increase the instrument LOD. (3) We characterized the NPOPR detection system

189 at different air flow rates (including 1.3, 2, 3, 4, and 5 L min^{-1}) and tested the conversion efficiency of O_3

190 by NO to NO_2 in the NO-reaction chamber at different NO mixing ratios and NO-reaction chamber

191 lengths. These efforts enabled us to better understand the running parameters of the NPOPR system and

192 perform data corrections under different air flow rates (see Sect. 2.2); (4) we tested the performance of

193 both the reaction and reference chambers by combining the field measurements and MCM modeling,

194 which indicated that reaction pathways of $P(O_3)$ and $D(O_3)$ and the radicals that play critical roles in

195 photochemical O_3 formation, such as HO_2, RO_2 and OH, reached quasi-steady states in approximately 3

196 min, thus ensuring that the lowest air residence time of 3.8 min (at an air flow rate of 5 L min^{-1}) in the

197 reaction and reference chambers was long enough to obtain accurate $P(O_3)_{net}$ values (see Sect. 3.2). These

198 efforts made the NPOPR system less prone to biases than other systems and increased its applicability.

199 **2.2 Characterization of the NPOPR detection system**

200 We characterized the NPOPR detection system following the same procedures as previous researchers,

201 including the residence time of the air, the wall losses of NO_2 and O_3, the transmittance of light and

202 temperature differences in the reaction and reference chambers, and the quantitative conversion

203 efficiency of O_3 to NO_2 (α) in the NO-reaction chamber. Additionally, we investigated the residence time

204 of the air and the wall losses of NO_2 and O_3 in the reaction and reference chambers at different flow rates

205 (including 1.3, 2, 3, 4, and 5 L min^{-1}) and the conversion efficiency of O_3 by NO to NO_2 in the NO-

206 reaction chamber at different NO mixing ratios and NO-reaction chamber lengths. The detailed

207 experimental performances and data analysis are shown in Appendix I, and the corresponding results are

208 described as follows.

209 ***The residence time.*** We tested the residence time of air in both chambers under different air flow

210 rates, including 1.3, 2, 3, 4, and 5 L min^{-1}, the obtained related residence time in the reaction chamber

211 were 0.35, 0.16, 0.11, 0.07, and 0.06 h, respectively. By setting different air flow rates, we were able to

212 obtain different residence time thus different limit of detection of NPOPR system, which make it

213 applicable to different ambient environment. To make sure that the mean residence time of air is the same

214 in the reaction and reference chambers, we also tested the residence time of air in the reference chamber

215 in parallel, which were not much difference with that in the reaction chamber, as shown in Table S1. The

216 experimental schematic diagram is shown in Fig. S2, the related results of different air flow rates are

217   shown in Fig. S3 and Table S1.

218   ***Wall losses of NO₂ and O₃.*** At air flow rates of 1.3, 2, 3, 4, and 5 L min⁻¹, the wall losses of O_3 in

219   the reaction chamber were found to be approximately 2 %, 0 %, 0 %, 0 %, and 0 %, respectively, and the

220   wall losses of O_3 in the reference chamber were found to be approximately 2 %, 1 %, 1 %, 0 %, and

221   0.7 %, respectively. While the wall losses of NO_2 in the reaction chamber at air flow rates of 1.3, 2, 3, 4,

222   and 5 L min⁻¹ were found to be approximately 4 %, 4 %, 2 %, 0 %, and 0.3 %, respectively, the wall

223   losses of NO_2 in the reference chamber were found to be approximately 2 %, 1 %, 0 %, 0 %, and 0. 6 %,

224   respectively. The experimental schematic diagram is shown in Fig. S4, and the related results of different

225   air flow rates are shown in Figs. S5-S6 and Tables S2-S5. We further compared the wall losses of O_3 and

226   NO_2 in the reaction and reference chambers at 5 L min⁻¹ with previous studies (as shown in Table S6)

227   and found that they were significantly smaller, but even with a flow rate of 1.3 L min⁻¹, the wall losses

228   were still smaller than 4 % and 2 % in the reaction chamber and the reference chambers, respectively.

229   We also tested the wall losses of NO_2 and O_3 in the chamber at a 5 L min⁻¹ flow rate at different humidities

230   of 35-75 %, the detailed results are shown in Fig. S7 and S8, which shows that the variation in humidity

231   effected the wall loss of NO_2 and O_3 by 0.03-0.12 % and 1.06-1.19 %, respectively, which is much

232   smaller than the instrument detection error (which is 2 % at ambient NO_2 mixing ratios of 0-100 ppb),

233   which indicates the small effects of Ox loss on $P(O_3)_{net}$ measurements in our NPOPR detection system.

234   ***The light transmittance and temperature differences in the reaction and reference chambers.*** It

235   is worth noting that there was still low transmittance of light ranging from 390 nm to 790 nm through

236   the UV protection film, and the reference chamber could not be regarded as completely dark; thus, we

237   tested the solar UV transmittance through the reaction and reference chambers of the NPOPR detection

238   system in the laboratory using a sunlight simulation lamp (SERIC XG-500B, Japan) to provide different

239   intensities of illumination. The photolysis frequencies of NO_2, O_3, HONO, H_2O_2, NO₃_M (photolysis of

240   NO_3 generates $NO+O_2$), NO₃_R (photolysis of NO_3 generates NO_2+O), HCHO_M (photolysis of HCHO

241   generates H_2+CO), and HCHO_R (photolysis of HCHO generates H+HCO) inside and outside the

242   reaction and reference chambers were measured using an actinic flux spectrometer (PFS-100; Focused

243   Photonics Inc., China). Table 1 presents the $J(NO_2)$, $J(O^1D)$, and $J(HONO)$ results for the outside and

244   inside chambers from this study and from the literature. $J(H_2O_2)$, $J(NO_3\_M)$, $J(NO_3\_R)$, $J(HCHO\_M)$,

245   and $J(HCHO\_R)$ are shown in Table S7.

246   The photolysis frequencies of all species inside the reaction chamber were in agreement with those

247   measured outside the reaction chamber within 4 %. Table S7 shows that the transmittivities of $J(H_2O_2)$,

248     $J(NO_3\_M)$, $J(NO_3\_R)$, $J(HCHO\_M)$, and $J(HCHO\_R)$ in the reaction chamber were more than 90 %.

249   However, we have observed that the transmittivities of $J(O^1D)$ were even higher than those of $J(HONO)$

250   (as shown in Table 1) in the reference chamber (which blocks sunlight at wavelengths < 390 nm),

251   theoretically, this is not possible according to JPL Publication 19-5 (Burkholder et al., 2020), where the

252   absorption cross section of HONO at wavelengths of 390-395 ranged from approximately $4.0\text{-}17.1 \times 10^{-21}$

253   cm^2, which is about two or three orders of magnitude higher than that of ozone (which ranged from

254   approximately $0.8\text{-}2.6 \times 10^{-23}$ cm^2 at wavelengths of 390-410 nm), and the photolysis quantum yield of

255   HONO at wavelengths of 390-395 is unity, which is about ten times higher than that of ozone (~ 0.08).

256   This will surely make the J values of HONO inside the reference chamber (which only has sunlight with

257   wavelengths > 390 nm) higher than that of ozone, according to the Eq. (S9). We also found that the

258   transmittivity of HONO and O_3 in the reference chamber obtained from the TUV simulation (as described

259   in Sect. 3.2) were 0.01 and 0, respectively, as shown in Table S13. Therefore, we believe the non-zero

260   measurement results of the transmittivity of O_3 shown in Table 1 and Table S7 are mostly probably due

261   to the instrument measurement error, this error is relatively large due to a limit number of measurement

262   points (3 points for each species). We further evaluated the measurement error of J values based on the

263   instrument measurement error of the actinic flux spectrometer, which can reach ± 5 % according to Bohn

264   et al. (2017), and re-evaluated the transmittivity error listed in Table 1 and Table S7 following the

265   procedures described in supplementary materials (Sect. 1.5). The calculation result from Eq. (S5) show

266   that the transmittivities errors are 0.07 for all species, within this error range, $J(O1D)$, $J(HONO)$, $J(H_2O_2)$,

267     $J(HCHO\_M)$, and $J(HCHO\_R)$ can be considered statistically indistinguishable from 0 in reference

268   chamber. However, $J(NO_2)$, $J(NO_3\_M)$, and $J(NO_3\_R)$ still distinctly positive values. Specifically, the

269   transmittivities of $J(NO_3\_M)$ and $J(NO_3\_R)$ of the reference chamber were more than 90 % (Table S7).

270   The influence of the measurement error of J values of all species on $P(O_3)_{net}$ will be discussed in Sect. 3.

271
272
273
274
275
276
277

Table 1. Transmittivities of photolysis frequency J (s⁻¹) values of different species in the reaction and reference chambers. The shaded and clear regions correspond to the transmittivities of J values in the reference (Ultem coated) and reaction (clear) chambers, respectively. The "transmittivities" column shows the transmittivities of the tested species from the measurements conducted with the set photolysis frequencies using SERIC XG-500B sunlight (this study) and ambient (literature). It should be noted that the errors listed here are relatively large and may not reliable due to a limit number of measurement points (3 points for each species). The calculated transmittivity errors are 0.07 for all species based on the ±5 % measurement error of the instrument.

	Transmittivities			
	Averaged (this study)	Cazorla *et al.*, 2010	Baier *et al.*, 2015	Sadanaga *et al.*, 2017
$J(NO_2)$	0.985 ±0.037	0.974	0.990	0.986
	0.094 ±0.014	0.021	0.01	0.121
$J(O^1D)$	1.020 ±0.04	0.991	0.978	1.030
	0.019 ±0.011	0.0058	0.001	~0
$J(HONO)$	0.983 ±0.037	0.976	0.982	0.988
	0.002 ±0.0002	0.0067	~0	0.017

We further detected the temperature in both the reaction and reference chambers when running the NPOPR system in an ambient observation campaign during November 2022 on the Panyu campus of Jinan University in Guangzhou, China (113° 36′ E, 23° 02′ N). We found that the UV protection Ultem film on the reference chamber did not block the heat outside the chamber, and the temperature remained the same in the reaction and reference chambers during the measurement test, as shown in Fig. S10.

The quantitative conversion efficiency of O₃ to NO₂ (α) in the NO-reaction chamber is crucial for accurate measurement of $P(O_3)_{net}$. Here, we used a perfluoroalkoxy (PFA) tube (outer diameter of 12.7 mm; inner diameter of 9.5 mm) as the NO-reaction chamber. The experimental schematic diagram is shown in Fig. S12. Known mixing ratios of O₃ and NO standard gas were introduced into the NO-reaction chamber, and NO reacted with O₃ to produce NO₂. To avoid the influence of small amounts of NO₂ impurity in the NO standard gas used for conversion, we added a cylinder filled with partialized crystals of FeSO₄·7H₂O to reduce NO₂ in the NO/N₂ gas cylinder to NO. We injected ~1800 ppbv NO into the NO-reaction chamber and tested the NO₂ mixing ratios from its outlet using a CAPS NO₂ monitor, as shown in Fig. S13. We found that the standard deviation of the NO₂ mixing ratios was lower than 0.027

302   ppbv, which is smaller than the baseline drifts of the CAPS (which were 0.043 and 0.030 ppbv (1 σ) at

303   integration times of 35 and 100 s, respectively, as mentioned in Sect. 2.3), so we believe the particulate

304   crystals of $FeSO_4 \cdot 7H_2O$ performed well and the potential bias introduced by the impurity in NO mixing

305   ratio for $P(O_3)_{net}$ was negligible. Finally, the total NO_2 mixing ratios, including that from the ambient air,

306   were measured using a CAPS NO_2 monitor ($[NO_2]_{CAPS}$). The O_3 mixing ratios were controlled at

307   approximately 310 ppbv according to the maximum mixing ratio range in the normal ambient atmosphere

308   (to ensure that all ambient and newly generated O_3 can react with NO and produce equivalent amounts

309   of NO_2). An O_3 generator equipped with a low-pressure mercury lamp was employed to generate O_3, and

310   the generated O_3 mixing ratios ($[O_3]_g$) were measured by a 2B O_3 monitor as mentioned above. Here, we

311   note that the O_3 mixing ratios were diluted by the added NO/N_2 gas (with a flow rate of 20 mL min^{-1}) in

312   the NO-reaction chamber (with a total flow rate of 1.11 L min^{-1}), taking 1800 ppbv NO/N_2 gas as an

313   example, the relationship between $[NO_2]_{CAPS}$ and $[O_3]_g$ can be described by Eq. (3):

314       $$[NO_2]_{CAPS} = \frac{1.09}{1.11}[O_3]_g \alpha \qquad\qquad\qquad (3)$$

315   To determine the optimal length of the NO-reaction chamber and NO mixing ratios, we performed

316   a cross test of α under the following scenarios: the NO-reaction chamber lengths were increased from 30

317   to 650 cm in 50 cm steps, and the NO standard gas (102.1 ppmv) was diluted to 600, 900, 1200, 1500,

318   1800, 2100, and 2400 ppbv in the NO reaction chamber. The results are shown in Fig. 2. We found that

319   at $[O_3]_g$ of approximately 310 ppbv, with NO mixing ratios ≥1800 ppbv in the NO reaction chamber, α

320   reached 99 %, 99.6 %, and 99.9 % with NO-reaction chamber lengths of 50, 70, and 100 cm, respectively,

321   where the corresponding O_3 residence times in the NO reaction chamber were 1.95, 2.74, and 3.91 s,

322   respectively. Considering both the optimal reaction time in the NO reaction chamber and α, we selected

323   the NO reaction chamber length as 100 cm with an NO mixing ratio of 1800 ppbv for the NPOPR

324   detection system.
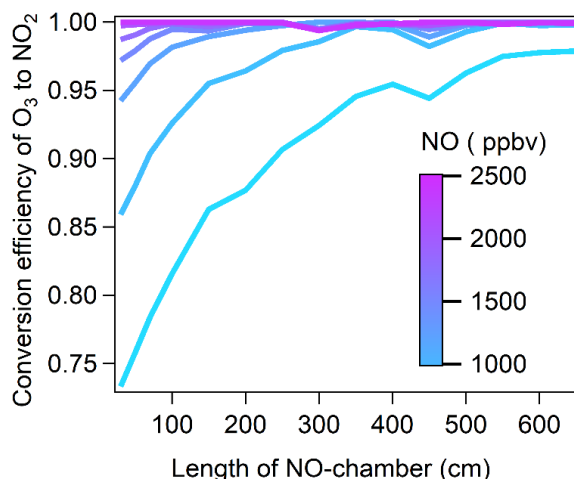
Figure 2: The conversion efficiency of O₃ by NO to NO₂ in the NO reaction chamber as a function of the NO chamber length, color coded by the NO mixing ratios.

The airtightness of the reaction and reference chambers We also checked the airtightness of the reaction and reference chambers by passing through gases with different flow rates based on the schematic diagram shown in Fig. S14 and compared the values of [air flow rate × pressure] between the inlet and outlet of the chambers (as indicated in Fig. 3). We found that the deviations in [air flow rate × pressure] at the inlet and outlet of the reaction and reference chambers at different flow rates were <3 % (as shown in Table S8), indicating the good airtightness of the reaction and reference chambers. This ensured that the photochemical reactions in the reaction and reference chambers would not be affected by the ambient air outside the chambers.
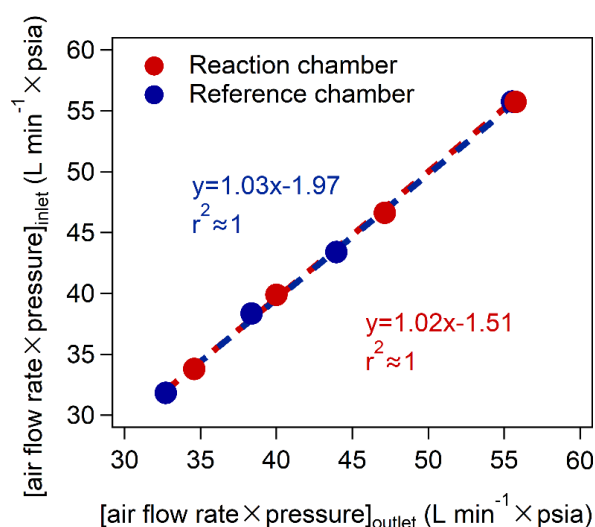
Figure 3: The relationship of the values of [air flow rate × pressure] between the inlet and outlet of the chambers (psia: Pounds Per Square Inch Absolute).

340

The flow states in the reaction and reference chambers We calculated the Reynolds number to check the gas flow state in the reaction and reference chambers. The Reynolds number (expressed as Eq. (4)) is a dimensionless number that can be used as the basis for judging the flow characteristics of a fluid:

$$Re = \rho v d / \mu \tag{4}$$

where v, ρ and μ are the flow velocity, density and viscosity coefficient of the fluid, respectively. In this study, the fluid is air, and d is the equivalent diameter of the reaction and reference chambers. The calculated Reynolds numbers in the two chambers under flow rates of 1.3, 2, 3, 4, and 5 L min^{-1} were 9.39, 14.58, 21.75, 29.05, and 36.34, respectively, indicating laminar flows in both chambers at different flow rates.

The HONO production in the reaction and reference chambers We tested the HONO production in the reaction and reference chambers under weather conditions similar to those during the SZMGT observations (humidity of 60-90% at a temperature of ~ 20 °C and $J(NO_2)$ of ~ 0-8 × 10^{-3} s^{-1}) at a 5 L min^{-1} sampling flow rate. We found that the HONO mixing ratios in the reaction and reference chambers were almost the same and not statistically different from that in the ambient air within the standard deviation, as shown in Fig. S9; therefore, we assumed that the HONO production in the reaction and reference chambers would not cause a significant difference in $P(O_3)_{net}$ in the two chambers. Unfortunately, we did not test HONO during the field observation period, but we have added the modeled HONO produced from the precursors before the ambient air was injected into the NPOPR system, as described in Sect. 3.2.

2.3 Calibration and measurement error of the CAPS NO$_2$ monitor

The Ox in the NPOPR detection system was measured by the CAPS NO$_2$ monitor. Detailed descriptions of this technique can be found elsewhere (Kebabian et al., 2008, 2005). We calibrated the CAPS NO$_2$ monitor using a NO$_2$ standard gas (with an original mixing ratio of 2.08 ppmv), which was first calibrated using the gas-phase titration method using NO standard gas and excessive O$_3$. The related experimental results are shown in Fig. S15. The detailed calibration procedure is as follows: a. injected ~ 10–100 ppbv of NO$_2$ standard gas for 30 min to passivate the surfaces of the monitor and then injected dry pure air for ~ 10 min to minimize the zero point drift, which were 0.043 and 0.047 ppbv at integration times of 35 and 100 s, respectively, and resulted in LODs of CAPS of 0.13 and 0.14 ppbv (3 σ), respectively; b.

369 injected a wide range of NO_2 mixing ratios (from 0–160 ppbv) prepared by mixing the NO_2 standard gas

370 with ultrapure air into the CAPS NO_2 monitor and repeated the experiments three times at each NO_2

371 mixing ratio. The final results are shown in Fig. 4. To check the baseline drift of the CAPS at different

372 humidities, we added another two sets of tests (as shown in Fig. S11) using ambient air and wet pure air

373 and found that (a) when injecting ambient air into the CAPS (RH ranged from ~30-35%), the baseline

374 drifts were 0.035 and 0.032 ppbv (1 σ) at integration times of 35 and 100 s, respectively; and (b) when

375 injecting wet pure air into the CAPS (RH ranged from 35-70%), the baseline drifts were 0.043 and 0.030

376 ppbv (1 σ) at integration times of 35 and 100 s, respectively. These baseline drifts were smaller than those

377 when injecting dry pure air to estimate the LOD of the CAPS. We chose the largest baseline drift when

378 injecting dry pure air to estimate the $P(O_3)_{net}$ error in the following analysis; by doing this, we were able

379 to include all the short-duration baseline drifting in the CAPS NO_2 monitor under different humidities.

380   To obtain an accurate measurement error of the CAPS NO_2 monitor (($O_{X_{CAPS}}$)$_{error}$), we fitted the

381 calibration results with a 68.3 % confidence level, and the blue line in Fig. 4 represents the maximum

382 fluctuation range under this confidence level. ($O_{X_{CAPS}}$)$_{error}$ was then calculated from the fluctuation

383 range of the 68.3 % confidence interval of the calibration curve. The relationship between ($O_{X_{CAPS}}$)$_{error}$

384 and the measured Ox value ([Ox]$_{measured}$) can be expressed as a power function curve, as shown in Eq.

385 (5):

386 $$(O_{X_{CAPS}})_{error} = 9.72 \times [O_X]_{measured}^{-1.0024} \tag{5}$$

387   Subsequent $P(O_3)_{net}$ error estimation according to the instrument measurement error of the CAPS

388 NO_2 monitor and the O_3 light-enhanced loss in the reaction and reference chambers are described in

389 Appendix II.
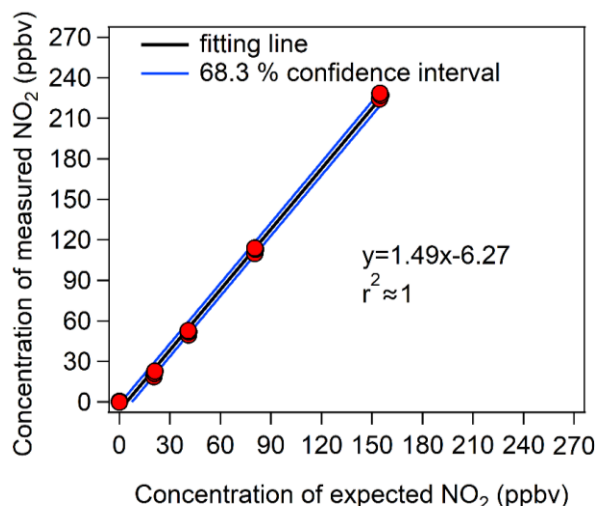
Figure 4: Calibration results of the CAPS NO_2 monitor with different NO_2 mixing ratios. The y-axis represents the NO_2 mixing ratios measured by the CAPS NO_2 monitor, and the x-axis represents the prepared NO_2 mixing ratios from the diluted NO_2 standard gas.

2.4 The measurement error of $P(O_3)_{net}$ and the LOD of the NPOPR detection system

To assess the measurement error of $P(O_3)_{net}$ and the LOD of the NPOPR detection system, dry pure air was introduced into the NPOPR detection system in sequence to adjust the system for ~ 2 h, followed by dry pure air or ambient air when the time resolution of the CAPS NO_2 monitor was 1 s and the integration time period was 100 s (the measurement durations for the reaction and reference chambers were both 2 min). The LOD of the NPOPR detection system was obtained as three times the measurement error of $P(O_3)_{net}$, which was determined at a time resolution of 4 min by propagating the errors of the O_x measured by the CAPS NO_2 monitor when ultrapure air or ambient air was introduced into the NPOPR detection system, combined with the related $\langle\tau\rangle$ under different flow rates, i.e., $\langle\tau\rangle$ was 0.063 h at a flow rate of 5 L min^{-1}. The detailed calculation method is shown in Eq. (6):

$$\text{LOD}=\frac{3\times\sqrt{([O_X]_{rea\_std})^2+([O_X]_{ref\_std])^2}}{\tau} \tag{6}$$

where $[O_X]_{rea\_std}$ and $[O_X]_{ref\_std}$ represent the standard deviation of O_X in the reaction and reference chambers measured by the CAPS NO_2 monitor with an integration time period of 100 s, respectively.

However, considering that the background Ox mixing ratios (measured by the CAPS NO_2 monitor of the air in the reference chamber) changed when measuring the ambient air, the measured O_X errors in the reaction and reference chambers changed with the Ox mixing ratios (as shown in Sect. 2.3), and the LOD must also be a function of the intrinsic ambient and photochemically formed O_3 and NO_2 mixing

411   ratios (i.e., the Ox mixing ratios measured by the CAPS NO_2 monitor). It is worth noting that the

412   measured O_X errors may also be influenced by the light-enhanced loss of O_3 in the reaction and reference

413   chambers under ambient conditions when the light intensity (especially $J(O^1D)$) and O_3 mixing ratios are

414   high, as tested and shown in Appendix II, but this effect is included in the measured O_X errors. Therefore,

415   when injecting ambient air into the NPOPR system, the error and LOD of $P(O_3)_{net}$ with a residence time

416   of τ can be calculated using Eq. (7) and Eq. (8), respectively:

417
$$P(O_3)_{net\_error}=\frac{\sqrt{(O_{X_\gamma})_{rea\_error}^2+((9.72\times[(O_X]_{rea\_measured}^{-1.0024}))_{rea\_std}^2+(O_{X_\gamma})_{ref\_error}^2+((9.72\times[(O_X]_{ref\_measured}^{-1.0024}))_{ref\_std}^2}}{\tau} \quad (7)$$

418     $LOD= 3\times P(O_3)_{net\_error}$ (8)

419   where $(O_{X_\gamma})_{rea\_error}$ and $(O_{X_\gamma})_{ref\_error}$ represent the measurement error caused by the light-enhanced loss

420   of O_3 in the reaction and reference chambers, respectively, and $(9.72\times[O_X]_{measured}^{-1.0024})_{rea\_std}$ and

421     $(9.72\times[O_X]_{measured}^{-1.0024})_{ref\_std}$ represent the standard deviation of O_X in the reaction and reference

422   chambers caused by the CAPS NO_2 monitor with an integration time period of 100 s, respectively. More

423   details about the $(O_{X_\gamma})_{rea\_error}$ and $(O_{X_\gamma})_{ref\_error}$ estimation method can be found in Appendix II.

424   In conclusion, the LOD of the NPOPR detection system is determined to be three times $P(O_3)_{net\_error}$,

425   where $P(O_3)_{net\_error}$ is mainly determined by the measurement error of Ox (including the Ox measurement

426   error of the CAPS NO_2 monitor, the light-enhanced loss of O_3, and the chamber Ox losses). Because the

427   measurement error of the CAPS NO_2 monitor decreases with increasing Ox mixing ratios (as shown in

428   Sect. 2.3), higher LODs could be obtained when injecting dry pure air into the NPOPR detection system,

429   which were approximately 0.07, 1.4, and 2.3 ppbv h^{-1} at air flow rates of 1.3, 3, and 5 L min^{-1}, respectively.

430   The results are summarized in Table S9.

431   During the field observations, the LOD values were highly dependent on the ambient conditions,

432   especially the light intensity and the Ox mixing ratios, and higher O_3 mixing ratios and lower light

433   intensity will likely result in lower LOD values.

434   **2.5 Laboratory tests of the NPOPR detection system**

435   We conducted an experiment in the laboratory to test the performance of the NPOPR detection system at

436   Jinan University Panyu Campus (23.0° N, 113.4° E) on 26 March 2021. Ambient air (5 L min^{-1}) was

437 simultaneously injected into the reaction and reference chambers of the NPOPR detection system in

438 parallel, and the sunlight simulation lamp mentioned above was used to simulate sunlight radiation. The

439 light intensities of the sunlight simulation lamp were decreased from 26000 cd to 0 cd in steps of 3700

440 cd, where cd indicates the light intensity SI unit candela. $P(O_3)_{net}$ was 28.6 ppbv h^{-1} at a light intensity of

441 26000 cd and gradually approached 0 ppbv h^{-1} at 0 cd (as shown in Fig. 5), indicating that the $P(O_3)_{net}$

442 change due to the different sunlight radiation could be well captured by the NPOPR detection system.
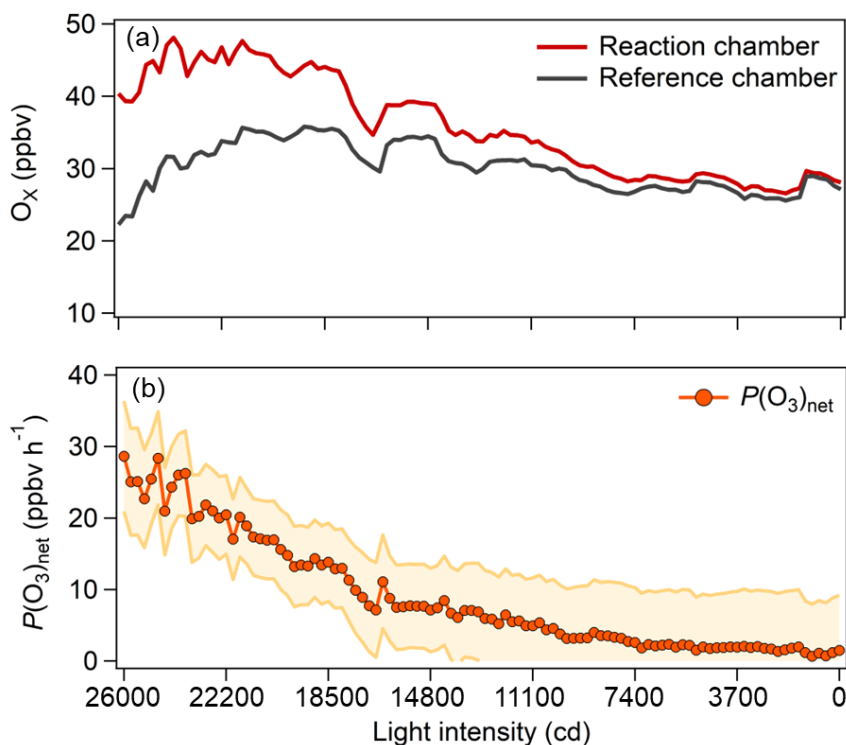
443

444 **Figure 5: (a) Measured Ox mixing ratios in the reaction and reference chambers and (b) the related $P(O_3)_{net}$**

445 **as a function of the light intensity during the experiment.**

446 **3 Atmospheric study and discussion**

447 **3.1 Field observations**

448 The self-built NPOPR detection system was employed in the field campaign conducted at SZMGT, which

449 is located in Shenzhen, China (as shown in Fig. S17), from 7 to 9 December 2021. During the campaign,

450 to achieve the lowest O_3 and NO_2 wall loss, we used a 5 L min^{-1} air flow rate in the reaction and reference

451 chambers (with a residence time of ~ 4 min). The photolysis frequencies of different species were

452 measured using the actinic flux spectrometer as mentioned above. O_3 and NO_X (NO+NO$_2$) mixing ratios

453 were measured using a 2B O_3 monitor and a chemiluminescence NOx monitor (Model 42i, Thermo

454   Fisher Scientific, USA), respectively. *T* and RH were measured by a portable weather station (Met Pak,

455   Gill Instruments Ltd, UK). Volatile organic compounds (VOCs) were measured by high-resolution

456   proton transfer reaction time-of-flight mass spectrometry (PTR-ToF-MS, Ionicon Analytik, Austria)

457   (Wang et al., 2020a; Wu et al., 2020) and an off-line gas chromatography mass spectrometry flame

458   ionization detector (GC–MS-FID) technique (Wuhan Tianhong, Co. Ltd, China) (Yuan et al., 2012)

459   (Table S11). Additionally, a self-built formaldehyde analyzer was used to detect formaldehyde (HCHO)

460   (Zhu et al., 2020). Figure 6 presents the temporal and diurnal variations in the $P(O_3)_{net}$, O_X, O_3, NO,

461   NO_2, NO_X, *T*, RH, $J(O^1D)$, and $J(NO_2)$ mixing ratios at SZMGT during the campaign.
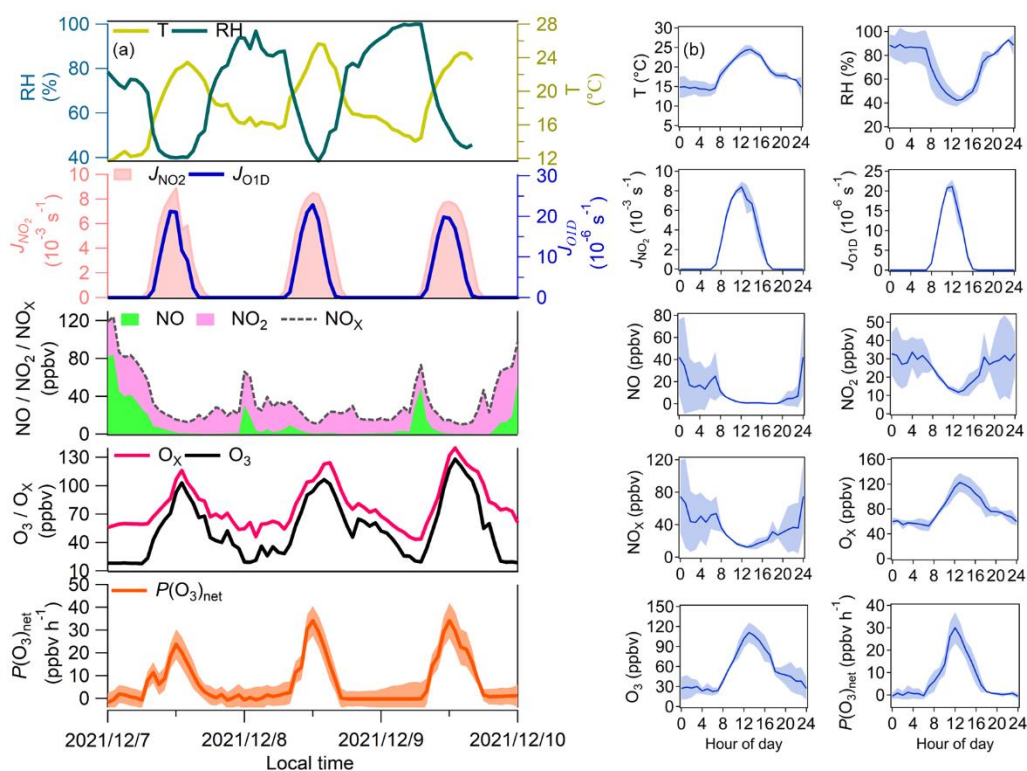
462

463   **Figure 6: (a) Time series and (b) average diurnal variations of $P(O_3)_{net}$, $J(NO_2)$, $J(O^1D)$, T, RH, O_X, NO_2 and**

464   **NO measured at SZMGT from 7 to 9 December 2021. The shaded areas represent the error of each measured**

465   **species, where the error of $P(O_3)_{net}$ was calculated according to the method described in Appendix II (the**

466   **estimation of the $P(O_3)_{net}$ error).**

467

468   During the measurement period, $P(O_3)_{net}$ ranged from ~ 0 to 34.1±7.8 ppbv h^{-1}, with an average

469   daytime (from 6:00–18:00) value of 12.8 (±5.5) ppbv h^{-1}. The maximum $P(O_3)_{net}$ at SZMGT was lower

470   than that measured in the urban area of Houston in the US (40–50 ppbv h^{-1} and 100 ppbv h^{-1} in autumn

471   and spring, respectively) (Baier et al., 2015; Ren et al., 2013), close to that measured in Indiana in the

472   US (~ 30 ppbv h^{-1} in spring) (Sklaveniti et al., 2018), and much higher than that measured at the

473   Wakayama Forest Research Station, a remote area of Japan (10.5 ppbv h^{-1} in summer) (Sadanaga et al.,

474   2017) and an urban area of Pennsylvania in the US (~ 8 ppbv h^{-1} in summer) (Cazorla et al., 2010). The

475   result indicates the rationality of the measured $P(O_3)_{net}$ in this study. From previous studies, the O_3

476   pollution in the PRD area is more severe in summer and autumn than in winter and spring (Zhang et al.,

477   2021). In this study, $P(O_3)_{net}$ was measured in wintertime, which was already high, so we believe that the

478   O_3 pollution of the PRD is severe and urgently needs to be controlled. More measurements of $P(O_3)_{net}$

479   worldwide are listed in Table S10, and we found that $P(O_3)_{net}$ was much higher in urban areas than in

480   remote areas using both modeling and direct measurement methods.

481   According to the diurnal variation in all the measured pollutant indicators, $P(O_3)_{net}$ started to

482   increase at approximately 7:00 local time, which may be due to two reasons: (1) the rise in O_3 precursors

483   (i.e., VOCs) due to the high-altitude atmospheric residual layer transported downward near the surface

484   at this time and (2) the increase in solar radiation intensity after 7:00, which increased the oxidation

485   capacity of the pollutants. These two factors jointly enhanced the photochemical oxidation reaction of

486   VOCs and gradually increased $P(O_3)_{net}$. $P(O_3)_{net}$ then peaked at approximately 12:0, which was consistent

487   with $J(NO_2)$, but this peak time was earlier than that of O_3, which peaked at approximately 14:00 , which

488   may be due to the photochemical reactions dominating O_3 mixing ratio changes between 12:00 and 14:00 .

489   After 14:00, the O_3 mixing ratios started to decrease, which may be due to other processes dominating

490   O_3 mixing ratio changes at this time, such as O_3 reacting with other pollutants or surface deposition and

491   the outflow of O_3 by physical transport. In conclusion, changes in O_3 mixing ratios were influenced by

492   both photochemical production and physical transport. Because HO_2 and RO_2 were not well captured in

493   the model, the simulations could lead to an underestimation of $P(O_3)_{net}$.

494   **3.2 Model simulation of $P(O_3)_{net}$ in the reaction and reference chambers**

495   **3.2.1 Modeling method**

496   To obtain a comprehensive understanding of the ozone production rate $P(O_3)$ and ozone destruction rate

497    $D(O_3)$ during the 4-min photochemical reaction in the reaction and reference chambers, we modeled

498    $P(O_3)$ and $D(O_3)$ at 12:00 on 7 December 2021 based on field observation data using a zero-dimensional

499   box model based on the Framework for 0-D Atmospheric Modeling (F0AM) v3.2 coupled with MCM

500   v3.3.1, which contains a total of 143 VOCs, more than 6700 species, involving more than 17000 reactions

501   (Jenkin et al., 2015). $P(O_3)_{net}$ can be expressed by the difference between $P(O_3)$ and $D(O_3)$, and $P(O_3)$

502   and $D(O_3)$ can be expressed as Eq. (9)–(10).

503    $$P(O_3)=k_{HO_2+NO}[HO_2][NO]+\sum_i k_{RO_{2,i}+NO}[RO_{2i}][NO]\varphi_i \tag{9}$$

504    $$D(O_3)=k_{O(^1D)+H_2O}[O(^1D)][H_2O]+k_{OH+O_3}[OH][O_3]+k_{HO_2+O_3}[HO_2][O_3]$$

505    $$+\sum_i \left(k_{O_3+Alkene_i}[O_3][Alkene_i]+k_{OH+NO_2}[OH][NO_2]+k_{RO_{2,i}+NO_2}[RO_{2i}][NO_2]\right) \tag{10}$$

506   where k_{M+N} represents the bimolecular reaction rate constant of M and N, and φ_i is the yield of NO$_2$ from

507   the reaction RO$_{2i}$ +NO. The relevant reaction rates of $P(O_3)$ and $D(O_3)$ and the VOC$_S$ mixing ratios during

508   7–9 December 2021 in SZMGT used in the model are listed in Tables 2 and S11.

509

510   **Table 2. O₃ production and destruction reactions and the relevant reaction rates used in the model.**

Reactions	Rate coefficient / unit	Number
O₃ production pathways - $P(O_3)$		
RO₂+ NO→RO + NO₂	$2.7\times10^{-12}\times exp(360/T)$ / molecules $^{-1}$ cm^3 s^{-1}	(R1)
HO₂+ NO→OH + NO₂	$3.45\times10^{-12}\times exp(270/T)$ / molecules $^{-1}$ cm^3 s^{-1}	(R2)
O₃ loss pathways - $D(O_3)$		
O₃ + hv → O¹D + O₂	Measured JO^1D / s^{-1}	(R3)
O₃ + C₂H₄ → HCHO + CH₂OOA	$9.1\times10^{-15}\times exp(-2580/T)$ / molecules $^{-1}$ cm^3 s^{-1}	(R4)
O₃ + C₃H₆ → CH₂OOB + CH₃CHO	$2.75\times10^{-15}\times exp(-1880/T)$ / molecules $^{-1}$ cm^3 s^{-1}	(R5)
O₃ + C₃H₆ → CH₃CHOOA + HCHO	$2.75\times10^{-15}\times exp(-1880/T)$ / molecules $^{-1}$ cm^3 s^{-1}	(R6)
O₃ + C₅H₈ → CH₂OOE + MACR	$3.09\times10^{-15}\times exp(-1995/T)$ / molecules $^{-1}$ cm^3 s^{-1}	(R7)
O₃ + C₅H₈ → CH₂OOE + MVK	$2.06\times10^{-15}\times exp(-1995/T)$ / molecules $^{-1}$ cm^3 s^{-1}	(R8)
O₃ + C₅H₈ → HCHO + MACROOA	$3.09\times10^{-15}\times exp(-1995/T)$ / molecules $^{-1}$ cm^3 s^{-1}	(R9)
O₃ + C5H₈ → HCHO + MVKOOA	$2.06\times10^{-15}\times exp(-1995/T)$ / molecules $^{-1}$ cm^3 s^{-1}	(R10)
O₃+ HO₂ → OH	$2.03\times10^{-16}\times (T/300)^{4.57}\times exp(693/T)$ / molecules $^{-1}$ cm^3 s^{-1}	(R11)
RO₂+ NO₂ → peroxy nitrates	$(3.28\times10^{-28}\times7.24\times10^{18}\times P/T\times(T/300)^{-6.87}\times1.125$ $\times10^{-11}\times(T/300)^{-1.105})\times10^{(log10(0.30)}/(1+(log10(2.93$ $\times10^{-17}\times7.24\times10^{18}\times P/T\times(T/300)^{-5.765})/0.75-1.27$ $\times log10(0.30))^2))/(2.926\times10^{-17}\times7.24\times10^{18}\times P/T$ $\times(T/300)^{-5.765})$ / molecules $^{-1}$ cm^3 s^{-1}	(R12)
NO₂+ OH → HNO₃	$3.2\times10^{-30}\times7.24\times10^{18}\times P/T\times(T/300)^{-4.5}\times3\times10^{-11}$ $\times10^{log10(0.41)}/(1+(log10(3.2\times10^{-30}\times7.24\times10^{18}\times P/T$ $\times(T/300)^{-4.5}/3\times10^{-11})/(0.75-1.27$ $\times(log10(0.41))^2)/(3.2\times10^{-30}\times7.24\times10^{18}\times P/T$ $\times(T/300)^{-4.5}+3\times10^{-11})$ / molecules $^{-1}$ cm^3 s^{-1}	(R13)
O₃+ OH → HO₂	$1.70\times10^{-12}\times exp(-940/T)$ / molecules $^{-1}$ cm^3 s^{-1}	(R14)

511   *The rate coefficient obtained from the MCM v3.3.1 model.

512   In total, three-stage simulations were carried out to obtain the 4-min photochemical reactions in

513 the reaction and reference chambers, and all three-stage models were operated in a time-dependent mode

514 with a 1 s resolution. In the 1st-stage, to establish a real atmospheric environment system, all observations

515 on 7 December 2021, 6:00-11:30, were used to constrain the model to obtain the mixing ratios of the

516 unmeasured species in the ambient atmosphere, including oxygenated VOCs (OVOCs, in total 16

517 species), non-methane hydrocarbons (in total 47 species), O_3, NO, NO_2, J values, T, RH, and pressure

518 (P). Because O_3-NO-NO_2 was not in a steady state when all species were constrained, we conducted a

519 2nd-stage simulation during 11:30–12:00. In this stage, we used the output mixing ratios of the

520 unmeasured species from the simulation in the last 1 s of the 1st-stage simulation as the input, which were

521 not constrained after providing initial values. For the measured species, O_3, NO, and NO_2 were no longer

522 constrained after providing initial values, while all other variables (including NO_X, VOCs, J values, RH,

523 T, P, etc.) were still constrained in a time-dependent mode with a 1 s resolution after providing initial

524 values. In the 3rd-stage, we modeled the 4-min photochemical reactions in the reaction and reference

525 chambers. We used the output mixing ratios of the unmeasured species (i.e., OH, HO_2, RO_2, SO_2, HONO,

526 etc.) from the simulation in the last 1 s of the 2nd-stage simulation and all measured values (i.e., O_3, NO,

527 NO_2, VOCs, J values, RH, T, P, etc.) as the model input, which were not constrained after providing

528 initial values. In addition, while maintaining the setup conditions for the 2nd-stage of the simulation, we

529 extended the simulation of the environment to 12:04 to obtain the modeled $P(O_3)_{net}$ in the environment

530 in the 3rd-stage simulation. The result is shown in orange marker in Fig. 10d. Figure 7 is an explicit

531 explanation of the 3rd-stage simulation in the reaction and reference chambers.
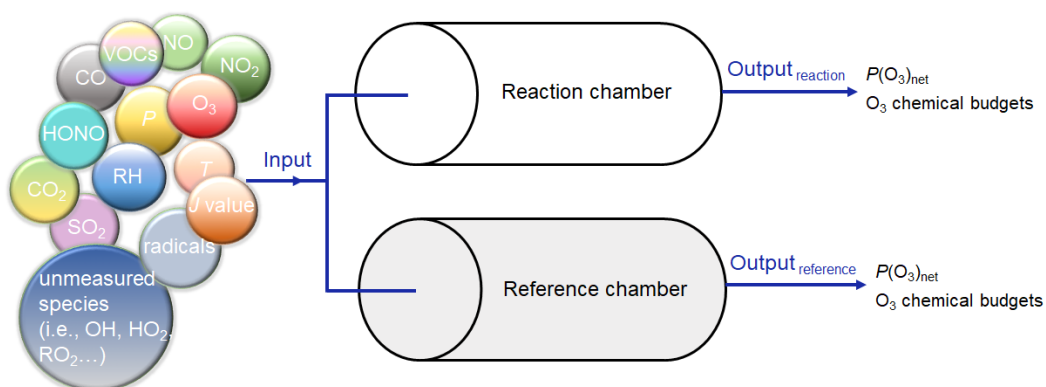
532

533 **Figure 7: Explicit explanation of the 3rd-stage model simulation (input meteorological conditions: P: 1015.3**

534 **hPa, T: 295.6 K, RH: 39.7 %).**

535   Specifically, because the photolysis frequencies play critical roles in the simulation of $P(O_3)_{net}$, the

536 J values obtained from two methods (labeled method I and method II) were used in the 3rd-stage 4-min

537 simulation. The J values used in method I were obtained from the measured values (including J(NO$_2$),

538 J(O^{1}D), J(HONO), J(H$_2$O$_2$), J(NO$_3$_M), J(NO$_3$_R), J(HCHO_M), and J(HCHO_R)) and the simulated values

539 using the Tropospheric Ultraviolet and Visible (TUV) radiation model (version 5.3) (including J(HNO$_3$),

540 J(CH$_3$CHO), J(MACR), J(MEK), J(HOCH$_2$CHO), J(C$_2$H$_5$CHO), J(C$_3$H$_7$CHO), and J(C$_4$H$_9$CHO).), while the J

541 values in method II were all obtained from the simulated values using the TUV model, detailed

542 information on these two methods is introduced in Appendix IV (Tables S12 and S13).

3.2.2 Radical chemistry in the reaction and reference chambers

544   The variations in the radical mixing ratios (i.e., HO$_2$, OH, RO$_2$) and NO$_3$, NO, NO$_2$, and O$_3$ mixing

545 ratios obtained from method I and method II during the 3rd-stage 4-min model simulation are shown in

546 Fig. 8 and Fig. S18, respectively. The production and destruction reactions of HO$_2$, OH, RO$_2$, and NO$_3$

547 in the reaction and reference chambers obtained from methods I and II are shown in Fig. 9 and Fig. S19,

548 respectively, the production and destruction reactions of RO$_X$ in the reaction and reference chambers

549 obtained from methods I and II are shown in Fig. S20, the detailed ROx production pathways of

550 NO$_3$+VOCs are shown in Fig. S21, and the final modeling results are shown in Fig. 10 and Fig. S22.

551   From Fig. 8, in the reaction chamber, the HO$_2$, OH, RO$_2$, and NO$_3$ concentrations first slightly

552 increased and then became stable, and their final concentrations were 2.00×10^8, 7.64×10^6, 1.08×10^8, and

553 8.47×10^6 molecules cm^{-3}, respectively. In the reference chamber, the HO$_2$ and RO$_2$ concentrations

554 dropped during the 1st half minute and rose afterward. The final HO$_2$ concentration (1.35×10^8 molecules

555 cm^{-3}) was lower than that in the reaction chamber, while the RO$_2$ concentration exceeded that in the

556 reaction chamber at the end of the 2nd minute and gradually became stable at 1.27×10^8 molecules cm^{-3}.

557 The OH concentration dropped significantly at the 1st minute and then became stable at approximately

558 6.16×10^5 molecules cm^{-3}. The NO$_3$ concentration rose significantly during the 4-min simulation and

559 reached 3.55×10^7 molecules cm^{-3} at the end, which was much higher than that in the reaction chamber.
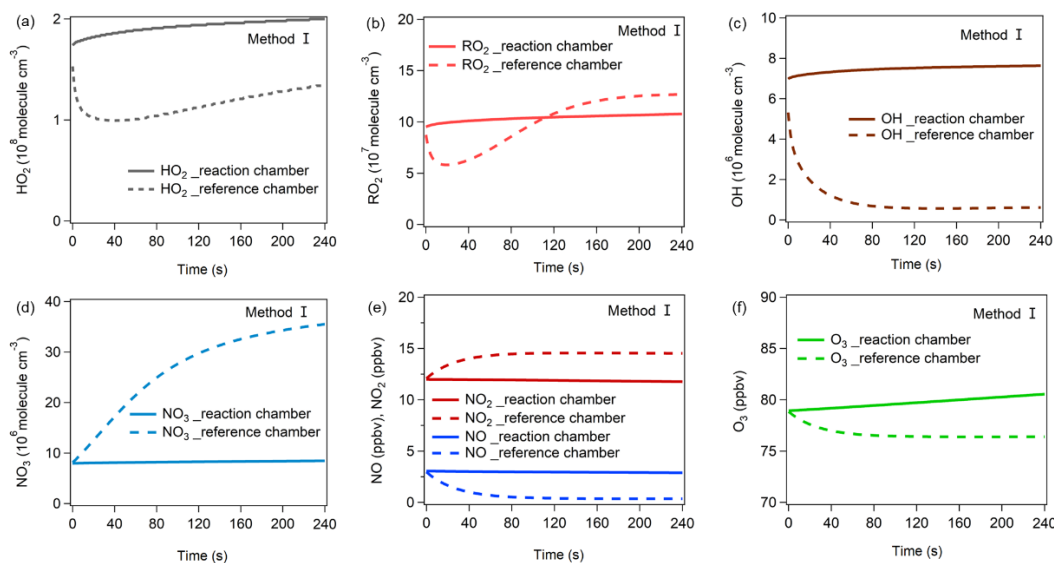
Figure 8: The variations of (a)HO$_2$, (b) RO$_2$, (c) OH, (d)NO$_3$, (e) NO, NO$_2$, and (f) O$_3$ mixing ratios during the 3rd-stage 4-min model simulation using method I. The mixing ratios changes of these items for method II is shown in Fig. S18.

OH, HO$_2$, RO$_2$, and NO$_3$ concentrations greatly impact the O$_3$ production and destruction rate. To better understand the factors that drive the OH, HO$_2$, RO$_2$, and NO$_3$ concentration changes, we have added their production and destruction pathways in Fig. 9. We found that the decrease in HO$_2$ and RO$_2$ concentrations in the reference chamber in the 1st half minute was mainly due to NO titration effects, as high NO mixing ratios existed during the 1st half minute. The increase in HO$_2$ concentrations afterward was largely attributable to RO+O$_2$ reaction/RO decomposition, OH+CO/VOCs reaction, OVOCs photolysis (i.e., C$_3$H$_4$O$_2$, C$_2$H$_2$O$_2$, C$_4$H$_6$O$_2$), and NO$_3$+VOCs reaction, and the increase in RO$_2$ concentrations afterward were largely attributable to OH+VOCs oxidation, OVOCs photolysis and O$_3$+VOCs reaction. The main OH sources in the reference chamber were both HO$_2$+NO in method I and method II. Due to sufficiently high J(NO$_3$) (~ 90% of that in the reaction chamber) and NO$_2$ concentrations in the reference chamber, the NO$_3$ photolysis and NO$_2$+NO$_3$ reaction consumed NO$_3$ in the reference chamber, but the NO$_3$ concentrations were still sufficiently high due to high production rates of NO$_3$ at the same time. The main NO$_3$ source in the reference chamber was the NO$_2$+O$_3$ reaction, followed by N$_2$O$_5$ decomposition. The NO concentrations were relatively high in the 1st minute and consumed NO$_3$ very quickly, but due to continuous NO$_3$ sources, the net NO$_3$ production rates (P(NO$_3$)$_{net}$) were positive (as shown in Fig. 9), which caused the NO$_3$ concentration to continue to increase (as shown in Fig. 8d). The main difference in NO$_3$ production in the reference chamber compared to that in the

 reaction chamber was the much higher N_2O_5 decomposition, which was mainly due to the high NO_2

582 concentrations in the reference chamber. On the other hand, although the $NO+NO_3$ reaction was also one

583 of the dominant NO_3 destruction pathways, NO_3 consumed by the $NO+NO_3$ reaction was significantly

584 smaller than NO_3 produced by the NO_2+O_3 reaction. Furthermore, in order to check if the NO_3+VOCs

585 reactions exists, we extracted all the $P(ROx)$ pathways related to NO_3+VOCs reactions during the 3rd-

586 stage 4-min model simulation in the reaction and reference chambers in method I, as shown in Fig. S20.

587 We found that the NO_3+VOCs reactions are mostly related to the OVOCs (i.e. 6-Ethyl-m-cresol and 3-

588 Ethyl-6-methylbenzene-1,2-diol) in Fig. S21. The production and destruction rates of ROx are shown in

589 Fig. S20.

590
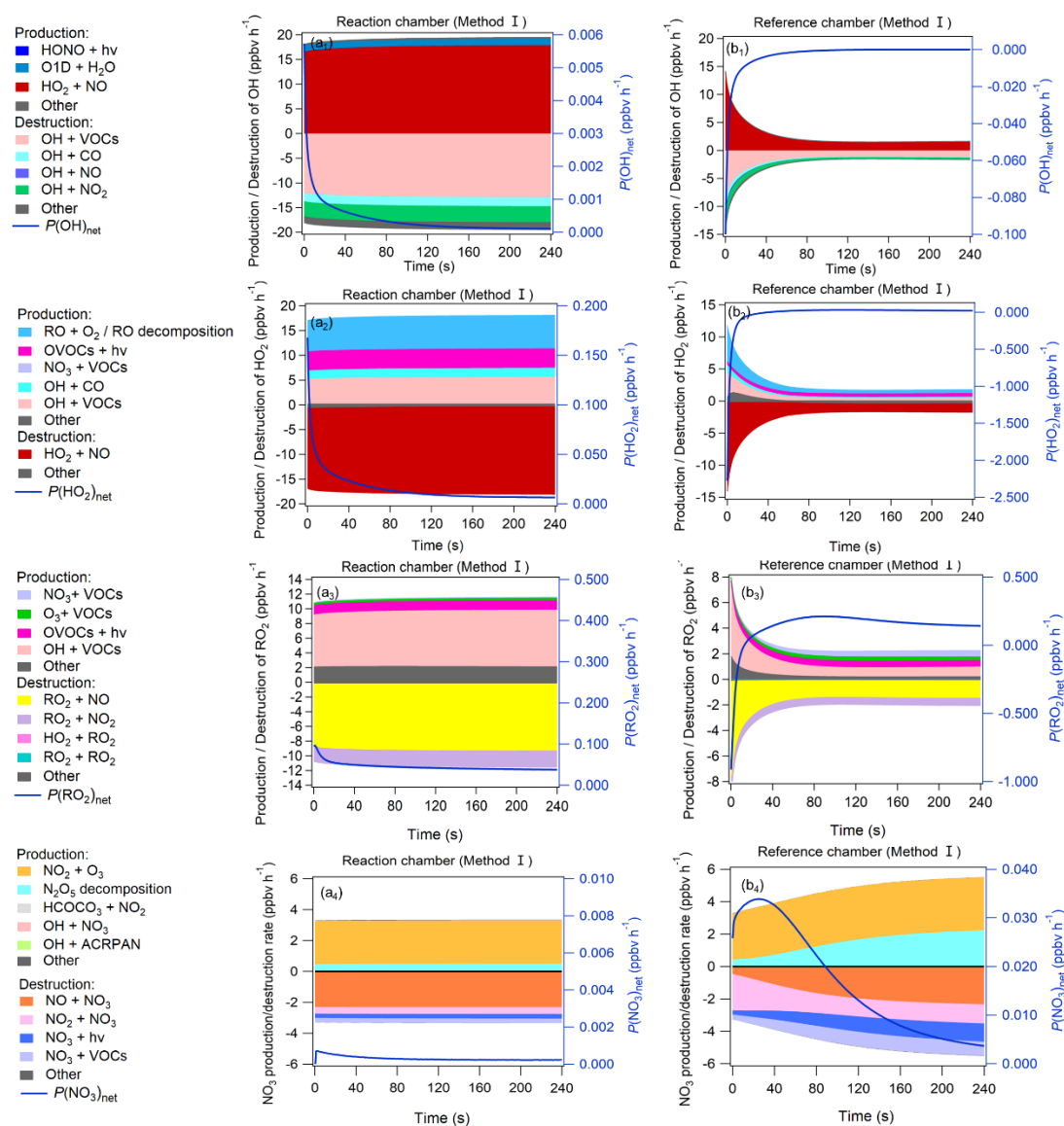
591
592 **Figure 9: Production and destruction pathways of OH (a_1-b_1), HO$_2$ (a_2-b_2), RO$_2$ (a_3-b_3), and NO$_3$ (a_4-b_4) during**

3.2.3 $P(O_3)_{net}$ formation and destruction pathways in the reaction and reference chambers

596   Figures 10a–d show the modeled $P(O_3)_{net}$ and the sources and sinks of various species during the

597 3rd-stage 4-min simulation. Figure 10a shows the steady state of $P(O_3)_{net}$ and the various species in the

598 ambient atmosphere achieved in the last 1 s of the 2nd-stage simulation; Figures 10b and c show the

599 modeled $P(O_3)_{net}$ and the O_3 chemical budgets in the reaction and reference chambers during the model

600 simulation period; Figure 10d summarizes the modeled $P(O_3)_{net}$ in the ambient air (represented as blue

601 and orange markers at the time when the ambient air was going in and out of the NPOPR system,

602 respectively) and the modeled $P(O_3)_{net}$ in the reaction and reference chambers. To compare the modeled

603 results with our measured results, we calculated the integral mean of the modeled $P(O_3)_{net}$ in the reaction

604 and reference chambers and appended the related measured $P(O_3)_{net}$ value during the 4-min simulation

605 time onto Fig. 10d (green maker). Furthermore, the reaction weights of different production and

606 destruction reaction processes of O_3 are shown in Figs. 10e–h.
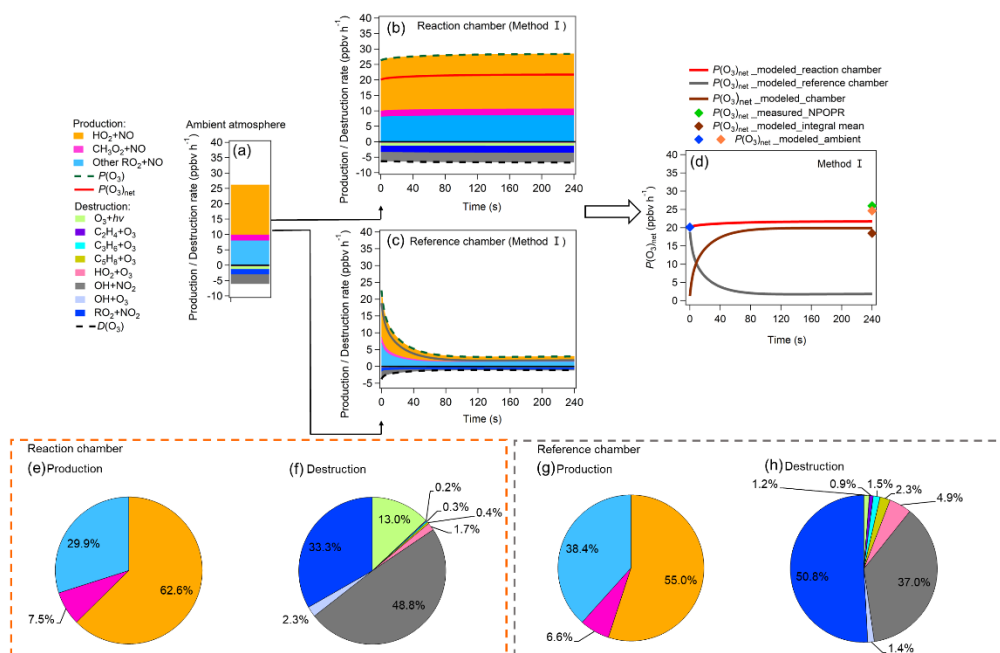
607

608 **Figure 10: (a)–(c) show the modeled $P(O_3)_{net}$ and the O_3 chemical budgets in (a) the ambient atmosphere when**
609 **injected into the reaction and reference chambers and (b–c) the reaction and reference chambers during the**
610 **4-min model simulation; (d) shows $P(O_3)_{net}$, where $P(O_3)_{net}$_modeled_ambient represent the modeled $P(O_3)_{net}$**
611 **in the ambient air at the time before (blue marker) and after (orange marker) the sampled ambient air was**
612 **injected   into   the   dual-channel   reaction   chamber. $P(O_3)_{net}$_modeled_reaction   chamber   and**
613 **$P(O_3)_{net}$_modeled_reference chamber represent the $P(O_3)_{net}$ changing trend during the 4-min photochemical**
614 **reactions   in   the   reaction   and   reference   chambers,   respectively, $P(O_3)_{net}$_modeled_chamber   =**

619   Figure 10a-h shows the contribution of different reaction pathways to $P(O_3)$ and $D(O_3)$. $P(O_3)$ and

620 $D(O_3)$ were almost the same within the 4-min reaction in the reaction chamber (all species reached a

621 steady-state condition), while $P(O_3)$ and $D(O_3)$ in the reference chamber decreased significantly within

622 the 1st min and remained stable in the following minutes. In the reaction chamber, the HO_2+NO reaction

623 contributed most to $P(O_3)$, accounting for 62.6 % of the total $P(O_3)$, with an integral mean value of 17.5

624 ppbv h^{-1} in the reaction chamber. The second important pathway of $P(O_3)$ was RO_2+NO (accounting for

625 37.4 % of the total $P(O_3)$). The reaction of RO_2+NO core presents more than approximately 1200 types

626 of RO_2 radicals, and the pathway of CH_3O_2+NO contributed 7.5 % of the total $P(O_3)$. The most important

627 contributor of $D(O_3)$ was OH+NO_2 (48.8 %), followed by RO_2+NO_2 (33.3 %), O_3 photolysis (13.0 %),

628 O_3+OH (2.3 %), O_3+HO_2 (1.7 %), C_5H_8+O_3 (0.4 %), C_3H_6+O_3 (0.3 %), and C_2H_4+O_3 (0.2 %). In the

629 reference chamber, the integral mean value of the HO_2+NO reaction was 2.3 ppbv h^{-1}, which had the

630 largest contribution to $P(O_3)$ (accounting for 55.0 %). The second largest contributor of $P(O_3)$ was

631 RO_2+NO (accounting for 45.0 % of the total $P(O_3)$), in which the pathway of CH_3O_2+NO contributed

632 6.6 % of the total $P(O_3)$. The most important contributor of $D(O_3)$ was RO_2+NO_2 (50.8 %), followed by

633 OH+NO_2 (37.0 %), O_3+HO_2 (4.9 %), C_5H_8+O_3 (2.3 %), C_3H_6+O_3 (1.5 %), O_3+OH (1.4 %), O_3 photolysis

634 (1.2 %), and C_2H_4+O_3 (0.9 %). For all $P(O_3)$ reactions, the weight of the RO_2+NO reaction in the

635 reference chamber was 7.5 % higher than that in the reaction chamber; however, for all $D(O_3)$ reactions,

636 the weight of the RO_2+NO_2 reaction in the reference chamber was 17.5 % higher than that in the reaction

637 chamber, which mitigates the high $P(O_3)$ caused by RO_2+NO in the reference chamber. Furthermore, the

638 weight of the OH+NO_2 reaction in the reference chamber was 11.9 % lower than that in the reaction

639 chamber, which may be the main reason that led to NO_2 mixing ratios in the reference chamber being

640 much higher than those in the reaction chamber. It is worth noting that the different reaction pathways of

641 $P(O_3)$ and $D(O_3)$ stabilized at approximately 1.5 min for both methods I and II (as shown in Figs. 10 and

642 S22), and the radicals that play critical roles in photochemical O_3 formation, such as HO_2, RO_2 and OH,

643 reached quasi-steady states in approximately 3 min (as shown in Figs. 8 and S18). As the lowest

644 experimental residence time in the reaction and reference chambers was 3.8 min at an air flow rate of 5

645 L min^{-1}, the photochemical reaction time at different air flow rates in the NPOPR system is sufficient for

646   investigating $P(O_3)_{net}$, and it is reasonable for us to set the alternate ambient air sampling time for the

647   reaction and reference chambers at 2 min, where the ambient air actually has already reacted for at least

648   3.8 min in the chambers.

649   The $P(O_3)_{net}$ value measured by the NPOPR detection system at 12:04 was 26.0 ppbv h^{-1}, which

650   was 1.4 ppbv h^{-1} higher than the modeled $P(O_3)_{net}$ value in the ambient air (orange marker in Fig. 10d,

651   24.6 ppbv h^{-1}) and 7.5 ppbv h^{-1} higher than the modeled $P(O_3)_{net}$ value of the NPOPR system (brown

652   marker in Fig. 10d, 18.5 ppbv h^{-1}, calculated from the integral mean of the 3rd-stage 4-min modeled

653    $P(O_3)_{net}$ in the reaction and reference chambers). Here, we note that for a better comparison between the

654   measured and modeled $P(O_3)_{net}$ values, the measured $P(O_3)_{net}$ used here was obtained from a 4-min time

655   resolution, which is 1.4 ppbv h^{-1} higher than the measured $P(O_3)_{net}$ value used in Fig. 6 (1-h time

656   resolution). The ratio of measured and modeled $P(O_3)_{net}$ values was 1.4, which is consistent with the

657   measured-to-modeled ratio of the cumulative $P(O_3)_{net}$ (1.3 and 1.4) obtained from previous studies

658   (Cazorla et al., 2012; Ren et al., 2013), where $P(O_3)_{net}$ values were also measured directly in the

659   atmosphere and were independent of the OH and HO$_2$ measurements. The reason for the difference

660   between the measured and modeled $P(O_3)_{net}$ here may be due to the inaccurate estimation of HO$_2$/RO$_2$

661   radicals; for example, Ren et al. (2013) found that $P(O_3)$ calculated from the modeled HO$_2$ was lower

662   than that calculated from the measured HO$_2$. The unknown HO$_2$ source should be identified for a more

663   accurate estimation of $P(O_3)_{net}$ in future studies.

664   Additionally, the modeled $P(O_3)_{net}$ using the J values obtained from method II was 9.3 ppbv h^{-1}

665   lower than the measured $P(O_3)_{net}$, and this discrepancy was slightly larger than that using method I, as

666   shown in Appendix IV (Fig. S22). The differences in the measured and modeled $P(O_3)_{net}$ by method I

667   and method II were 28.8 % and 35.8 %, respectively. This difference was mainly due to the transmittance

668   of $J(NO_2)$ in method II (30 %) being much higher than that in method I (9 %), and NO$_2$ photolysis

669   products were involved in the main reaction of O$_3$ production of HO$_2$+NO and RO$_2$+NO, so the modeled

670    $P(O_3)_{net}$ in the reference chamber was slightly overestimated in method II, thus leading to an

671   underestimation of the final $P(O_3)_{net}$.

672   Furthermore, because the NO$_2$ data used here were measured by a commercially available

673   chemiluminescence NOx monitor, the NO$_2$ and NOx mixing ratios would be overestimated due to NOz

674   interference (i.e., HNO$_3$, PANs, HONO, etc.) (Dunlea et al., 2007). According to our test, the

675   chemiluminescence technique could bias NO_2 by 5 % compared to the CAPS technique, which is

676   regarded as a trustworthy NO_2 measurement technique without chemical interference. Therefore, we

677   simulated the interference of NO_2 measured by a chemiluminescence NOx monitor in method I as follows:

678   reducing and increasing the ambient NO_2 mixing ratios by 5 % in the 3rd-stage 4-min simulation in the

679   reaction and reference chambers. The results show that increasing and decreasing NO_2 by 5 % resulted

680   in a decrease in $P(O_3)_{net}$ by 1.64 % and 3.68 %, respectively (as shown in Fig. S23), which is much

681   smaller than the bias caused by $P(O_3)_{net}$ in the reference chambers (which were 13.9 % and 22.3 % for

682   method I and method II, respectively). To evaluate $P(O_3)_{net}$ error caused by the measurement error of J

683   values, we introduced a ±5 % error to the measured J values during the 3rd stage of the 4-min simulation

684   in method I. The modeled $P(O_3)_{net}$ results are presented in Fig. S24 in the supplementary materials. We

685   observed that the inclusion of a -5 % measurement error in J values led to a decrease in $P(O_3)_{net}$ by

686   7.27 %, while adding a +5 % measurement error in J values caused an increase in $P(O_3)_{net}$ by 3.08 %.

687   This implies that the maximum bias of $P(O_3)_{net}$ caused by the measurement error of J values falls within

688   the error range of the currently assessed $P(O_3)_{net}$ error, which was 13.9 % for method I. Therefore, we

689   conclude that this type of error will not influence our final modeling results and conclusions.

690   In conclusion, modeling tests demonstrated that the radicals and gas species in the reaction

691   chamber of the NPOPR detection system were similar to those in genuine ambient air, while these

692   radicals also unexpectedly existed in the reference chamber. This was mainly because the UV protection

693   film used by the reference chamber did not completely filter out sunlight, which led to the low

694   transmittance of light ranging from 390 nm to 790 nm. The $P(O_3)_{net}$ biases caused by this interference

695   modeled in method I and method II were 13.9 % and 22.3 %, respectively, which ensured that the

696   measured $P(O_3)_{net}$ by the NPOPR detection system should be regarded as the lower limit values of real

697     $P(O_3)_{net}$ in the atmosphere. We recommend that the J values obtained from method I should be used in

698   the model simulation, which can better explain the photochemical formation of O_3 in the actual

699   atmosphere, but if direct J value measurements cannot be achieved during field observations, the J values

700   obtained from method II would also be acceptable in modeling studies.

701   **4 Conclusions**

702   We modified and improved a net photochemical ozone production rate (NPOPR) detection system based

703   on a dual-channel reaction chamber technique, which provides more accurate results and has broader

704   application potential compared to previous studies. The main improvements of NPOPR detection system

705   compared to previous studies were as follows: (1) improved the design of the reaction and reference

706   chambers to make sure they have good airtightness; (2) changed the air sampling structure to enable the

707   total air flow rates change freely from 1.3 to 5 L min^{-1} in the reaction and reference chambers, which can

708   make the NPOPR system achieve different limits of detection (LODs) and appliable to different ambient

709   environment; (3) characterized the NPOPR detection system at different air flow rates to optimize the

710    $P(O_3)_{net}$ measurements, the LODs of the NPOPR detection system are 0.07, 1.4, and 2.3 ppbv h^{-1} at air

711   flow rates of 1.3, 3, and 5 L min^{-1}, respectively; (4) tested the performance of both reaction and reference

712   chambers by combining the field measurement and the MCM modeling method.

713   The NPOPR detection system was employed in the field observation at the Shenzhen

714   Meteorological Gradient Tower (SZMGT), which is located in PRD, China. During the measurement

715   period, the $P(O_3)_{net}$ was around zero during nighttime and ranged from ~ 0 to 34.1±7.8 ppbv h^{-1} during

716   daytime (from 6:00–18:00), with the average value of 12.8 (±5.5) ppbv h^{-1}. Besides, $P(O_3)_{net}$ start to

717   increase at around 7:00 at local time, this may be due to the rise of the O_3 precursors (i.e., VOCs)

718   transported down from the high-altitude atmospheric residual layer to the near-surface and the increase

719   of solar radiation intensity increased the atmospheric oxidation capacity. $P(O_3)_{net}$ was then reaches a peak

720   at around 12:00 at noon time, by coupling with diurnal O_3 mixing ratios trends, we confirmed that the

721   ground-level O_3 mixing ratios were influenced by both photochemical production and physical transport.

722   In order to clarify the detailed photochemical reaction processes in the reaction and reference

723   chambers of NPOPR system, we modeled the $P(O_3)_{net}$ on 7 December 2021, 12:00-12:04 in the reaction

724   and reference chambers using MCM v3.3.1. As the photolysis frequencies of different species (J values)

725   play critical roles in the formation of $P(O_3)_{net}$, the J values obtained from two methods were used in the

726   4-min chamber photochemical reaction (labeled as method I and method II), in method I , eight main J

727   values (e.g., $J(NO_2)$, $J(O^1D)$, $J(HONO)$, etc.) were measured directly, and other J values were obtained

728   from the simulated values using the Tropospheric Ultraviolet and Visible (TUV) radiation model, while

729   in method II, J values were all obtained from the simulated values using TUV model (as described in

730   Sect. 3.2). Modeling tests demonstrated that the mixing ratios of different radicals and gas species (i.e.,

731   OH, HO$_2$, RO$_2$, NO$_3$, NO, NO$_2$, and O$_3$) in the reaction chamber were similar with those in the real

ambient environment, while due to the UV protection film used by the reference chamber does not completely filter out the sunlight, there was low transmittance of the light ranged from 390 nm to 790 nm. In the reaction chamber, the contribution of different reactions to $P(O_3)$ and $D(O_3)$ modeled by method I and II were quite similar, where the HO_2+NO reaction contributed most to $P(O_3)$ (~ 62.6 %), followed by the RO_2+NO reaction (~ 37.4 %). The $OH+NO_2$ reaction contributed most to $D(O_3)$, which accounted for ~ 48.9 %, followed by the RO_2+NO_2 reaction O_3 photolysis, which accounted for ~ 33.3 % and 13.0 %, respectively. In the reference chamber, the contribution of different reactions to $P(O_3)$ and $D(O_3)$ modeled by method I and II were different, where the HO_2+NO reaction contributed ~ 55.0 % and ~ 58.2 % to the total $P(O_3)$, respectively, and RO_2+NO contributed ~ 44.9 % and 41.8 % to the total $P(O_3)$, respectively. The most important contributor of $D(O_3)$ modeled by method I was RO_2+NO_2 (50.8 %), followed by $OH+NO_2$ (37.0 %), while the most important contributor of $D(O_3)$ modeled by method II was $OH+NO_2$ (46.8 %), followed by RO_2+NO_2 (44.1 %). For all $P(O_3)$ reactions, the weight of RO_2+NO reaction in the reference chamber was 7.5 % and 4.3 % higher than that in the reaction chamber in method I and II, respectively, however, for all $D(O_3)$ reactions, the weight of RO_2+NO_2 reaction in the reference chamber was 17.5 % and 10.9 % higher than that in the reaction chamber in method I and II, respectively, which will somehow mitigate the high $P(O_3)$ caused by RO_2+NO in the reference chamber. The different reaction pathways of $P(O_3)$ and $D(O_3)$ had stabilized at around 1.5 min, and the radicals that play critical roles in photochemical O_3 formation, such as HO_2, RO_2 and OH, reached quasi-steady states in about 3 min, the long enough ambient air residence time in the reaction and reference chambers ($\geq$ 3.8 min) make the photochemical reaction time at different air flow rates in the NPOPR system sufficient enough for investigating the $P(O_3)_{net}$, and it is reasonable for us to set the alternate ambient air sampling time for the reaction and reference chambers at 2 min, where the ambient air actually has already reacted for at least 3.8 min in the chambers.

The biases of the modeled $P(O_3)_{net}$ caused by the interference of the reactions in the reference chamber in method I and method II were 13.9 % and 22.3 %, respectively; thus, the measured $P(O_3)_{net}$ by the NPOPR detection system should be regarded as the lower limit values of the real $P(O_3)_{net}$ in the atmosphere. Nevertheless, the measured $P(O_3)_{net}$ values were 7.5 and 9.3 ppbv h^{-1} higher than the modeled $P(O_3)_{net}$ values obtained from methods I and II, respectively, which may be due to the inaccurate modeling of HO_2/RO_2 radicals. Short-lived intermediate measurements coupled with direct $P(O_3)_{net}$

measurements are needed in future study in order to studies to better understand the photochemical

production and destruction mechanisms of O_3. We recommend that the J values obtained from method I

should be used in the model simulation, which can better explain the photochemical formation of O_3 in

the actual atmosphere, but if direct J value measurements cannot be achieved during field observations,

the J values obtained from method II would also be acceptable in modeling studies.

The self-built NPOPR detection system in this study filled the gap in the observation method in

China. The research results not only help us to understand the tropospheric O_3 budget but also provide

an important data basis for formulating correct O_3 pollution prevention measures and control strategies.

Data availability. The observational data used in this study are available from corresponding authors

upon request (junzhou@jnu.edu.cn).

Author contributions. JZ, BY, and MS designed the experiment, YXH and JZ developed and assembled

the NPOPR detection system, YXH, JZ, JPZ, BY, YW, YFW, SCY, YWP, JPQ, XJH, XS and YBC

collected and analyzed the data YXH and JZ wrote the manuscript, all authors revised the manuscript.

Competing interests. The authors declare that they have no known competing interests.

Acknowledgements. This study was funded by the Key-Area Research and Development Program of

Guangdong Province (grant no. 2020B1111360003), and the Natural Science Foundation of Guangdong

Province (grant no. 2020A1515110526). We thank Nan Ma and Xiaofeng Su for the HONO production

experiment.

References

Avnery, S., Mauzerall, D. L., Liu, J., and Horowitz, L. W.: Global crop yield reductions due to surface

ozone exposure: 1. Year 2000 crop production losses and economic damage, Atmos. Environ., 45,

2284-2296, https://doi.org/10.1016/j.atmosenv.2010.11.045, 2011.

Baier, B. C., Brune, W. H., Lefer, B. L., Miller, D. O., and Martins, D. K.: Direct ozone production rate

measurements and their use in assessing ozone source and receptor regions for Houston in 2013, Atmos.

Environ., 114, 83-91, http://dx.doi.org/10.1016/j.atmosenv.2015.05.033, 2015.

Baier B C, Brune W H, Miller D O, et al., Higher measured than modeled ozone production at increased

NOx levels in the Colorado Front Range, Atmos. Chem. Phys., 17: 11273–11292,

789   https://doi.org/10.5194/acp-17-11273-2017, 2017.

790   Bell, M. L., McDermott, A., Zeger, S. L., Samet, J. M., and Dominici, F.: Ozone and short-term mortality

791   in 95 US urban communities, J. Am. Med. Assoc. 1987-2000., 292, 2372-

792   2378, https://doi.org/10.1001/jama.292.19.2372, 2004.

793   Berman, J. D., Fann, N., Hollingsworth, J. W., Pinkerton, K. E., Rom, W. N., Szema, A. M., Breysse, P.

794   N., White, R. H., and Curriero, F. C.: Health benefits from large-scale ozone reduction in the United

795   States, Environ. Health. Persp., 120, 1404-10, https://doi.org/10.1289/ehp.1104851, 2012.

796   Bohn B, Lohse I. Calibration and evaluation of CCD spectroradiometers for ground-based and airborne

797   measurements of spectral actinic flux densities. Atmos. Meas. Tech., 10, 3151–3174,

798   https://doi.org/10.5194/amt-10-3151-2017, 2017.

799   Burkholder, J., Sander, S., Abbatt, J., Barker, J., Cappa, C., Crounse, J., Dibble, T., Huie, R., Kolb, C.,

800   and Kurylo, M.: Chemical kinetics and photochemical data for use in atmospheric studies, evaluation

801   number 19, Pasadena, CA: Jet Propulsion Laboratory, National Aeronautics and

802   Space Administration, 2020, http://jpldataeval.jpl.nasa.gov. 2020.

803   Cazorla, M., Brune, and W. H.: Measurement of ozone production sensor, Atmos. Meas. Tech., 3, 545-

804   555, https://doi.org/10.5194/amt-3-545-2010, 2010.

805   Cazorla, M., Brune, W. H., Ren, X., and Lefer, B.: Direct measurement of ozone production rates in

806   Houston in 2009 and comparison with two estimation methods, Atmos. Chem. Phys., 12, 1203-1212,

807   https://doi.org/10.5194/acp-12-1203-2012, 2012.

808   Dunlea, E. J., Herndon, S. C., Nelson, D. D., Volkamer, R. M., Martini, F. S., Sheehy, P. M., Zahniser,

809   M. S., Shorter, H., Wormhoudt, J. C., Lamb, B. K., Allwine, E. J., Gaffney, J. S., Marley, N. A., Grutter,

810   M., Marquez, C., Blanco, S., Cardenas, B., Retama, A., Villegas, C. R. R., Kolb, C. E., Molina, L. T.,

811   and Molina, M. J.: Evaluation of nitrogen dioxide chemiluminescence monitors in a polluted urban

812   environment, Atmos. Chem. Phys., 7, 2691–2704, https://doi.org/10.5194/acp-7-2691-2007, 2007.

813   Jenkin, M. E., Young, J. C., and Rickard, A. R.: The MCM v3.3.1 degradation scheme for isoprene,

814   Atmos. Chem. Phys., 15, 11433-11459, https://doi.org/10.5194/acp-15-11433-2015, 2015.

815   Kanaya, Y., Tanimoto, H., Yokouchi, Y., Fumikazu Taketani, F. T., Komazaki, Y., Irie, H., Takashima, H.,

816   Pan, X., Nozoe, S., and Inomata, S.: Diagnosis of photochemical ozone production rates and limiting

817   factors in continental outflow air masses reaching Fukue Island, Japan: ozone-control implications,

818   Aerosol. Air. Qual. Res., 16, 430-441, https://doi.org/10.4209/aaqr.2015.04.0220, 2016.

819   Karakatsani, A., Kapitsimadis, F., Pipikou, M., Chalbot, M. C., Kavouras, I. G., Orphanidou, D., Papiris,

820   S., and Katsouyanni, K.: Ambient air pollution and respiratory health effects in mail carriers, Environ.

821   Res., 110, 278-85, https://doi.org/10.1016/j.envres.2009.11.002, 2010.

822   Lee, S.-B., Bae, G.-N., Lee, Y.-M., Moon, K.-C., and Choi, M.: Correlation between light intensity and

823   ozone formation for photochemical smog in urban air of seoul, Aerosol. Air. Qual. Res., 10, 540-549,

824   https://doi.org/10.4209/aaqr.2010.05.0036, 2010.

825   Liu, S. C.: Possible effects on froposheric O3 and OH due to NO emissions, Geophys. Res. Lett., 4,

826   325-328, https://doi.org/10.1029/GL004i008p00325, 1977.

827   Liu, X., Wang, N., Lyu, X., Zeren, Y., Jiang, F., Wang, X., Zou, S., Ling, Z., and Guo, H.: Photochemistry

828   of ozone pollution in autumn in Pearl River Estuary, South China, Sci. Total Environ., 754, 141812,

829   https://doi.org/10.1016/j.scitotenv.2020.141812, 2020.

830   Luecken, D. J., Phillips, S., Sarwar, and G., Jang, C.: Effects of using the CB05 vs. SAPRC99 vs. CB4

831   chemical mechanism on model predictions: Ozone and gas-phase photochemical precursor

832   concentrations, Atmos. Environ., 42, 5805-5820, https://doi.org/10.1016/j.atmosenv.2007.08.056,

833   2008.

834   Lu, K., Zhang, Y., Su, H., Brauers, T., Chou, C. C., Hofzumahaus, A., Liu, S. C., Kita, K., Kondo, Y,

835   Shao, M., Wahner, A., Wang, J., Wang, X., and Zhu, T.: Oxidant (O3+ NO2) production processes and

836   formation   regimes   in   Beijing,   J.   Geophys.   Res.   Atmos.,   115,   D07303,

837   https://doi.org/10.1029/2009JD012714, 2010.

838   Malley, C. S., Henze, D. K., Kuylenstierna, J. C. I., Vallack, H. W., Davila, Y., Anenberg, S. C., Turner,

839   M. C., and Ashmore, M. R.: Updated global estimates of respiratory mortality in adults ≥30 years of

840   age   attributable   to   long-term   ozone   exposure,   Environ.   Health.   Persp.,   125,   087021,

841   https://doi.org/10.1289/EHP1390, 2017.

842   Martinez, M.: OH and HO2 concentrations, sources, and loss rates during the Southern Oxidants Study

843   in   Nashville,   Tennessee,   summer   1999,   J.   Geophys.   Res.-Atmos.,   108,   4617,

844   https://doi.org/10.1029/2003JD003551, 2003.

845   Mazzuca, G. M.,Ren, X., Loughner, C. P., Estes, M., Crawford, J. H., Pickering, K. E., Weinheimer, A.

846   J., and Dickerson, R. R.: Ozone production and its sensitivity to NOx and VOCs: results from the

847   DISCOVER-AQ field experiment, Houston 2013, Atmos. Chem. Phys., 16, 14463-14474,

848   https://doi.org/10.5194/acp-16-14463-2016, 2016.

849 Mills, G., Sharps, K., Simpson, D., Pleijel, H., Broberg, M., Uddling, J., Jaramillo, F., Davies, W. J.,

850   Dentener, F., Van den Berg, M., Agrawal, M., Agrawal, S. B., Ainsworth, E. A., Buker, P., Emberson,

851   L., Feng, Z., Harmens, H., Hayes, F., Kobayashi, K., Paoletti, E., and Van Dingenen, R.: Ozone

852   pollution will compromise efforts to increase global wheat production, Glob. Chang. Biol., 24, 3560-

853   3574, https://doi.org/10.1111/gcb.14157, 2018.

854 O'Neill, M. S., Jerrett, M., Kawachi, I., Levy, J. I., Cohen, A. J., Gouveia, N., Wilkinson, P., Fletcher, T.,

855   Cifuentes, L., Schwartz, J.: Health, wealth, and air pollution: advancing theory and methods, Environ.

856   Health. Persp., 111, 1861-70, https://doi.org/10.1289/ehp.6334, 2003.

857 Pan, X.; Kanaya, Y., Tanimoto, H., Inomata, S., Wang, Z., Kudo, S., and Uno, I.: Examining the major

858   contributors of ozone pollution in a rural area of the Yangtze River Delta region during harvest season,

859   Atmos. Chem. Phys., 15, 6101-6111, https://doi.org/10.5194/acp-15-6101-2015, 2015.

860 Ren, X., van Duin, D., Cazorla, M., Chen, S., Mao, J., Zhang, L., Brune, W. H., Flynn, J. H., Grossberg,

861   N., Lefer, B. L., Rappenglück, B., Wong, K. W., Tsai, C., Stutz, J., Dibb, J. E., Thomas Jobson, B.,

862   Luke, W. T., and Kelley, P.: Atmospheric oxidation chemistry and ozone production: results from

863   SHARP 2009 in Houston, Texas, J. Geophys. Res.-Atmos., 118, 5770-5780,

864   https://doi.org/10.1002/jgrd.50342, 2013.

865 Sadanaga, Y., Kawasaki, S., Tanaka, Y., Kajii, Y., and Bandow, H.: New system for measuring the

866   photochemical ozone production rate in the atmosphere, Environ. Sci. Technol., 51, 2871-2878,

867   https://doi.org/10.1021/acs.est.6b04639, 2017.

868 Shen, H., Liu, Y., Zhao, M., Li, J., Zhang, Y., Yang, J., Jiang, Y., Chen, T., Chen, M., Huang, X., Li, C.,

869   Guo, D., Sun, X., Xue, L., and Wang, W.: Significance of carbonyl compounds to photochemical ozone

870   formation in a coastal city (Shantou) in eastern China, Sci. Total. Environ., 764, 144031,

871   https://doi.org/10.1016/j.scitotenv.2020.144031, 2021.

872 Sklaveniti, S., Locoge, N., Stevens, P. S., Wood, E., Kundu, S., and Dusanter, S.: Development of an

873   instrument for direct ozone production rate measurements: measurement reliability and current

874   limitations, Atmos. Meas. Tech., 11, 741-761, https://doi.org/10.5194/amt-11-741-2018, 2018.

875 Tadic, I., Crowley, J. N., Dienhart, D., Eger, P., Harder, H., Hottmann, B., Martinez, M., Parchatka, U.,

876   Paris, J.-D., Pozzer, A., Rohloff, R., Schuladen, J., Shenolikar, J., Tauer, S., Lelieveld, J., and Fischer,

877   H.: Net ozone production and its relationship to nitrogen oxides and volatile organic compounds in the

878   marine boundary layer around the Arabian Peninsula, Atmos. Chem. Phys., 20, 6769-6787,

879   https://doi.org/10.5194/acp-20-6769-2020, 2020.

880   Wang, C., Yuan, B., Wu, C., Wang, S., Qi, J., Wang, B., Wang, Z., Hu, W., Chen, W., Ye, C., Wang, W.,

881   Sun, Y., Wang, C., Huang, S., Song, W., Wang, X., Yang, S., Zhang, S., Xu, W., Ma, N., Zhang, Z.,

882   Jiang, B., Su, H., Cheng, Y., Wang, X., and Shao, M.: Measurements of higher alkanes using NO+

883   chemical ionization in PTR-ToF-MS: important contributions of higher alkanes to secondary organic

884   aerosols in China, Atmos. Chem. Phys., 20, 14123–14138, https://doi.org/10.5194/acp-20-14123-

885   2020, 2020a.

886   Wang, F., An, J., Li, Y., Tang, Y., Lin, J., Qu, Y., Chen, Y., Zhang, B., and Zhai, J.: Impacts of uncertainty

887   in AVOC emissions on the summer ROx budget and ozone production rate in the three most rapidly-

888   developing economic growth regions of China, Adv. Atmos. Sci., 31, 1331-1342,

889   https://doi.org/10.1007/s00376-014-3251-z, 2014.

890   Wolfe, G. M., Marvin, M. R., Roberts, S. J., Travis, K. R., and Liao, J.: The Framework for 0-D

891   Atmospheric Modeling (F0AM) v3.1, Geosci. Model. Dev., 9, 3309-3319,

892   https://doi.org/10.5194/gmd-9-3309-2016, 2016.

893   Wu, C., Wang, C., Wang, S., Wang, W., Yuan, B., Qi, J., Wang, B., Wang, H., Wang, C., Song, W., Wang,

894   X., Hu, W., Lou, S., Ye, C., Peng, Y., Wang, Z., Huangfu, Y., Xie, Y., Zhu, M., Zheng, J., Wang, X.,

895   Jiang, B., Zhang, Z., and Shao, M.: Measurement report: Important contributions of oxygenated

896   compounds to emissions and chemistry of volatile organic compounds in urban air, Atmos. Chem.

897   Phys., 20, 14769–14785, https://doi.org/10.5194/acp-20-14769-2020, 2020.

898   Yuan, B., Chen, W., Shao, M., Wang, M., Lu, S., Wang, B., Liu, Y., Chang, C.-C., and Wang, B.:

899   Measurements of ambient hydrocarbons and carbonyls in the Pearl River Delta (PRD), China, Atmos.

900   Res., 116, 93-104, https://doi.org/10.1016/j.atmosres.2012.03.006, 2012.

901   Zhang, A., Lin, J., Chen, W., Lin, M., and Lei, C.: Spatial-temporal distribution variation of ground-level

902   ozone in China's Pearl River Delta metropolitan region, Int. J. Environ. Res. Public Health., 18, 872,

903   https://doi.org/10.3390/ijerph 18030872, 2021.

904   Zhou, W., Cohan, D. S., and Henderson, B. H.: Slower ozone production in Houston, Texas following

905   emission reductions: evidence from Texas Air Quality Studies in 2000 and 2006, Atmos. Chem. Phys.,

906   14, 2777-2788, https://doi.org/10.5194/acp-14-2777-2014, 2014.

907   Zhu, M., Dong, H., Yu, F., Liao, S., Xie, Y., Liu, J., Sha, Q., Zhong, Z., Zeng, L., Zheng, J.: A new

908   portable instrument for online measurements of formaldehyde: from ambient to mobile emission

909   sources. Environ. Sci. Technol. Lett, 7, 292-297, https://dx.doi.org/10.1021/acs.estlett.0c00169, 2020.

910   Zou, Y., Deng, X. J., Zhu, D., Gong, D. C., Wang, H., Li, F., Tan, H. B., Deng, T., Mai, B. R., Liu, X. T.,

911   and Wang, B. G.: Characteristics of 1 year of observational data of VOCs, NOX and O3 at a suburban

912   site in Guangzhou, China. Atmos. Chem. Phys., 15, 6625-6636, https://doi.org/10.5194/acp-15-6625-

913   2015, 2015.